On the dynamic response of adhesively bonded structures

Maria Lißner[a,*], Enrique Alabort[a,b], Borja Erice[e], Hao Cui[c], Bamber R. K. Blackman[d], Nik Petrinic[a]

[a] Department of Engineering Science, University of Oxford, Parks Road, Oxford, OX1 3PJ, United Kingdom
[b] Oxmet Technologies Ltd., Unit 15, Oxford Industrial Park, Yarnton, OX5 1QU, United Kingdom
[c] School of Aerospace, Transport and Manufacturing, Cranfield University, Bedford, MK43 0AL, United Kingdom
[d] Department of Mechanical Engineering, Imperial College, London, SW7 2AZ, United Kingdom
[e] Department of Structural Engineering, NTNU, Trondheim, 7491, Norway

ABSTRACT

Fracture mechanics experiments are used to investigate the rate-dependent failure of adhesively bonded structures under different deformation modes: I, II and I/II. First, the high-rate mechanical response of the adhesive interface is analysed with a newly developed method – which relies entirely upon digital image correlation. The method was purposely designed to avoid any dynamic effects which may be present. This novel method is verified against quasi-static standard methods showing good agreement. Finally, simulations of the experiments are used to validate a cohesive zone model of the adhesive. The ability of the model to predict cohesive failure under a wide range of strain rates and deformation modes is demonstrated.

1. Introduction

Hybrid material combinations, such as composite-metal adhesive joints, are increasingly employed in several industries where energy efficiency improvements rely upon weight reduction whilst maintaining the structural integrity [1]. Understanding the failure performance for each material individually is key for establishing failure design and criteria for hybrid structures. The fracture energy,J, and the failure strength are material parameters of paramount importance for the optimal design of these structures. Accurate experimentation is critical in the identification of the failure sequence of adhesively bonded structures. However, most of the experimental methods available in the literature lack accuracy – particularly when high strain rates and impact events are involved [2].

Several studies have investigated the failure strength of adhesive joints under quasi-static and dynamic loading conditions [3–14]. In quasi-static loading conditions, typical butt joints [6,9] and ring specimens [4] have been used to investigate the failure strength in the normal direction to the adhesive interface. For the shear loading behaviour, adhesive joints are commonly tested using the single lap joints (SLJ) [10] and double lap joints (DLS) [8]. Most dynamic investigations employ hydraulic testing machines or the Split Hopkinson Bar (SHB). The SHB is used extensively to measure the dynamic failure strength of adhesive joints [3,5,6,9,12–14]. Other studies have employed the SHB with SLJ [15], pin-collar-specimens [3], torsion specimens [7] and cubic specimens [13,14] to investigate the adhesive strength under shear deformation. Others have investigated the failure strength of the adhesive in normal direction to the adhesive interface using butt joints [6,9], hat-shaped butt joints [5] and cubic joints [11,12]. All these investigations obtained a strong dependence of the mechanical response of adhesive joints on the applied strain rate. Moreover, studies have encountered heat dissipation during the damage process of the adhesive joint in dynamic loading environments which is believed to be dependent on the strain rate [12,13,16]. Nevertheless, the strain and displacement measurements remain critical when analysing the strain and displacement based on the SHB analysis. It is believed that high-speed cameras in combination with digital image correlation (DIC) increases the accuracy of the relevant adhesive interfaces measurements [17].

Most methods for deriving the fracture energy were developed with quasi-static observations in mind. However, adhesively bonded structures are also subjected to dynamic loading. In those cases, one requires understanding of the performance of the adhesive in rate-dependent environments. Few investigations have focussed on understanding the fracture energy behaviour as a function of the loading rate [18–21]. Isakov *et al.* used wedge DCB experiments (WDCB) to obtain the fracture energy by measuring the compliance [20]. Others have employed strain gauges attached to the beam to calculate the force over the bending strain [21], thus allowing the use of classical methods to obtain the fracture energy. For ENF experiments, researchers have measured

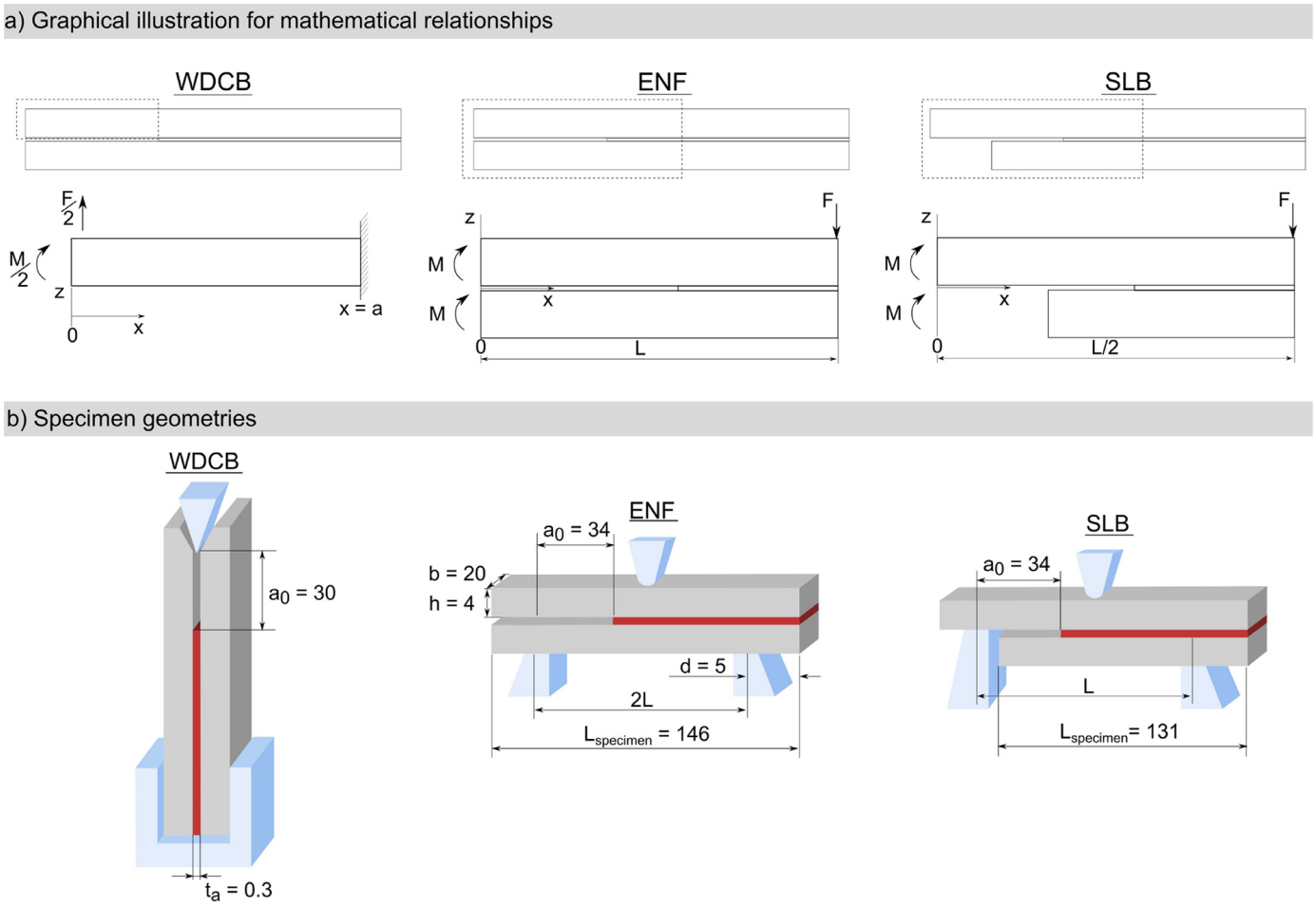

Fig. 1. (a) Graphical illustration of the used orientation and nomenclature used to derive the mathematical relationships and (b) the WDCB, ENF and SLB adhesive joint fracture specimens.

the fracture energy by extracting the force from the strain gauge data and the displacement using high-speed cameras in the Split Hopkinson bar [18,19]. However, signal filtering is required in order to obtain a suitable force-displacement response to derive the fracture energy. Moreover, the calculation of the fracture energy under dynamic loading employing the aforementioned techniques needs careful consideration. Dynamic effects such as inertia and oscillation of the beams should be considered – if those are not negligible, the measurements may lack accuracy.

With the above in mind, this paper presents a new method to identify the mechanical performance of the adhesive interface dependent on rate and mode of fracture. Firstly, quasi-static and high-rate experiments for three different fracture modes: mode I, mode II and mixed-mode I/II are carried out using the WDCB, ENF and SLB test specimens respectively. Secondly, a new measurement technique is employed to derive the high-rate force-displacement curves. Thirdly, the quasi-static measurements are compared to traditional analyses, thus validating the new approach. Finally, the quasi-static and high-rate experiments are simulated using a finite element methods. The models employ a cohesive zone model developed previously by the authors [15]. Experimental results are used to validate the cohesive zone model and to compare; (i) the ability of the model to predict failure; and (ii) the validity of the developed experimental technique to measure adhesively bonded structures under different rate- and mode-dependent environments.

2. Background

Many researchers have investigated different ways to measure the fracture energy of adhesive interfaces using fracture mechanics experiments under different fracture modes [22–26]. The double cantilever beam (DCB) is generally used to investigate the mechanical performance of the adhesive interface normal to its surface [22,23,26–30], while the end notched flexure (ENF) resolves the adhesive's response tangential to its surface [24,26,31–33]. The single leg beam (SLB) is usually employed to reveal the adhesive's mechanical performance under more complex stress states [25,26]. The DCB is believed to be of more relevant practical importance, but in practice, a pure fracture mode does not exist. All of these methods have one thing in common: one needs to measure the crack length during the failure process to calculate the fracture energy by means of beam theory. For this, several approaches have been developed: (i) measuring the crack length directly by crack length monitoring [22,27,34–36] or (ii) estimating the crack length by measurement of the compliance [33,37–39]. However, the calculation of the fracture energy is challenging when relying upon monitoring of the crack length.

Unfortunately, a few studies [40–43] have experienced unstable crack propagation which prevents a clear observation of the crack tip. Moreover, clear visibility of the crack is difficult for certain adhesives. This can have a non-negligible effect on the compliance derived from the crack length in the classic compliance calibrated method (CCM) [44]. Also, when using ductile adhesive systems, the energy dissipated at the fracture process zone (FPZ) can be large [32] – this can influence the accuracy of the results. The calculation of the fracture energy –

based on beam theory – is underestimated when the aforementioned effects are ignored. Thus, improved approaches have been developed to correct the calculation, for example by the use of direct beam theory (DBT) [45] or corrected beam theory (CBT) [46]. However, those methods also rely upon the accurate measurement of the crack length – this is challenging, even more so at high strain rates. De Moura *et al.* introduced the compliance based beam method (CBBM) [33] to avoid the need to measure the actual crack length propagation. This approach relies entirely upon the compliance performance during the failure process. This method considers the FPZ which is formed due to multiple micro-crack nucleations within the adhesive thickness and plastification of the adhesive. Using this approach, the dissipated energy in the FPZ of ductile adhesives is considered in the final result of the fracture energy. Other researchers based their crack length measurement on digital image correlation (DIC) recordings to avoid the difficult crack length monitoring [47,48].

For the calculation of the force-displacement responses of WDCB, ENF and SLB specimens the CBBM is considered to account for the FPZ. Using the CBBM approach, a direct measurement of the crack length is not required. Based on simple beam theory and Timoshenko beam theory, the mathematical relationships necessary for calculating the crack length can be derived. Therefore one only needs to monitor the applied load and displacement during the experiment. The following equations are used for our analysis method and are presented and summarised here for the reader's convenience. Fig. 1(a) provides an overview of the orientation and nomenclature used for generating the mathematical relationships for each specimen configuration.

Based on simple beam theory (SBT) and considering Timoshenko beam theory – to account for shear effects – the strain energy Π for the WDCB experiments can be deduced from

$$\Pi = 2\left[\int_0^a \frac{M^2}{2EI}dx + \int_0^a \int_{-\frac{h}{2}}^{\frac{h}{2}} \frac{\tau^2}{2G}bdzdx\right] \tag{1}$$

where M is the bending moment, h is the thickness, E is the Young's modulus, G is the shear modulus of the adherent, I is the second moment of inertia, and τ is the shear stress which is determined following

$$\tau = \frac{3}{2}\frac{V}{bh}\left(1 - \frac{y^2}{c^2}\right) \tag{2}$$

where V is the shear force, and $c = h/2$. Using the Castelgiano theorem following

$$u = \frac{d\Pi}{dF} \tag{3}$$

where u is the displacement, and F is the vertical force, the WDCB compliance can be calculated employing

$$F(u) = \frac{u}{C} \tag{4}$$

and

$$C(\mathrm{a}) = \frac{8\mathrm{a}^3}{\mathrm{Ebh}^3} + \frac{12\mathrm{a}}{5\mathrm{bhG}} \tag{5}$$

where G is the shear modulus of the adherent. For the ENF and SLB specimens, the strain energy Π can be written as

$$\Pi = \int_0^{2L} \frac{M^2}{2EI}dx + \int_0^{2L}\int_{-h}^{h} \frac{\tau^2}{2G}bdzdx. \tag{6}$$

Thus, the compliance C for the ENF [33] and SLB [25] experiments can be obtained using

$$C(\mathrm{a}) = \frac{3\mathrm{a}^3 + 2\mathrm{L}^3}{8\mathrm{bh}^3\mathrm{E}} + \frac{3\mathrm{L}}{10\mathrm{bhG}} \tag{7}$$

and

$$C(\mathrm{a}) = \frac{28\mathrm{a}^3 + \mathrm{L}^3}{32\mathrm{Ebh}^3} + \frac{3(\mathrm{a} + \mathrm{L})}{20\mathrm{Gbh}} \tag{8}$$

respectively, where E is the Young's modulus, b the specimen width, h the thickness of the adherent, G the shear modulus, a the crack length and L the characteristic specimen length.

Finally, the applied force is determined using Eq. (4) and considering that C involves the total compliance of both adherents. The force, displacement and crack length results can then be utilised to generate the fracture energy for each fracture mode. Although, the intention of this paper is to provide force-displacement data sets for quasi-static and high-rate loading regimes in order to prove the validity of a cohesive zone model developed, the equations for the fracture energy are provided for further comparison. The fracture energy for the WDCB experiments, J_{Ic}, can be calculated using [49]

$$J_{\mathrm{Ic}}(\mathrm{a},\mathrm{F}) = \frac{12\mathrm{a}^2}{\mathrm{Eh}^3\mathrm{b}^2}\mathrm{F}^2 + \frac{\mathrm{F}}{\mathrm{b}}(\mathrm{w}_1^{'} - \mathrm{w}_2^{'}) \tag{9}$$

where $w_1^{'}$ and $w_2^{'}$ are the beam rotations.

The fracture energy, J_{IIc}, for the ENF specimens was obtained using the approach of the equivalent crack length a_e [33]. The quasi-static measurements a_e is calculated as

$$a_{\mathrm{e}} = \left[\frac{C_c}{C_{0c}}a_0^3 + \frac{2}{3}\left(\frac{C_c}{C_{0c}} - 1\right)L^3\right]^{\frac{1}{3}} \tag{10}$$

with

$$C_{\mathrm{c}} = C - \frac{3L}{10bhG} \quad and \quad C_{0c} = C_0 - \frac{3L}{10bhG} \quad . \tag{11}$$

The fracture energy can then be fully described using the flexural modulus E_f. E_f is calculated following

$$E_{\mathrm{f}} = \frac{3a_0^3 + 2L^3}{8bh^3}\left(C_0 - \frac{3L}{10bhG}\right)^{-1}. \tag{12}$$

The flexure modulus can then be employed to calculate the fracture energy following

$$J_{\mathrm{IIc}}(\mathrm{a_e},\mathrm{F}) = \frac{9\mathrm{F}^2\mathrm{a_e}^2}{16\mathrm{b}^2\mathrm{h}^3\mathrm{E_f}}. \tag{13}$$

Accordingly, the fracture energy for the SLB configuration, $J_{I/IIc}$, can be calculated using

$$J_{\mathrm{I/IIc}}(\mathrm{a},\mathrm{F}) = \frac{21\mathrm{F}^2\mathrm{a}^2}{16\mathrm{E_f}\mathrm{b}^2\mathrm{h}^3} + \frac{3\mathrm{F}^2}{10\mathrm{Gb}^2\mathrm{h}} \tag{14}$$

while the normal and tangential components are described following

$$J_{\mathrm{Ic}}(\mathrm{a},\mathrm{F}) = \frac{12\mathrm{F}^2\mathrm{a}^2}{16\mathrm{E_f}\mathrm{b}^2\mathrm{h}^3} + \frac{3\mathrm{F}^2}{10\mathrm{Gb}^2\mathrm{h}} \tag{15}$$

and

$$J_{\mathrm{IIc}}(\mathrm{a},\mathrm{F}) = \frac{9\mathrm{F}^2\mathrm{a}^2}{16\mathrm{E_f}\mathrm{b}^2\mathrm{h}^3} \tag{16}$$

respectively. The SLB fracture energy is then fully defined for the quasi-static loading case using Eqs. (4) and (8).

3. Experimental methods

3.1. Adherent and adhesive materials

The thermosetting epoxy film adhesive AF 163-2OST from Scotch-Weld™ was used to bond two titanium alloy Ti–6Al–4V adherents. The film adhesive is supported with a glass fibre carrier mat which enables improved handling for large scale applications. Different sample geometries were designed and manufactured to measure fracture properties under three different loading modes: The wedge double cantilever beam (WDCB) specimen was used to study the mechanical performance of the adhesive interface when loaded normal to the adhesive surface (mode I). The shear behaviour (mode II) was experimentally studied

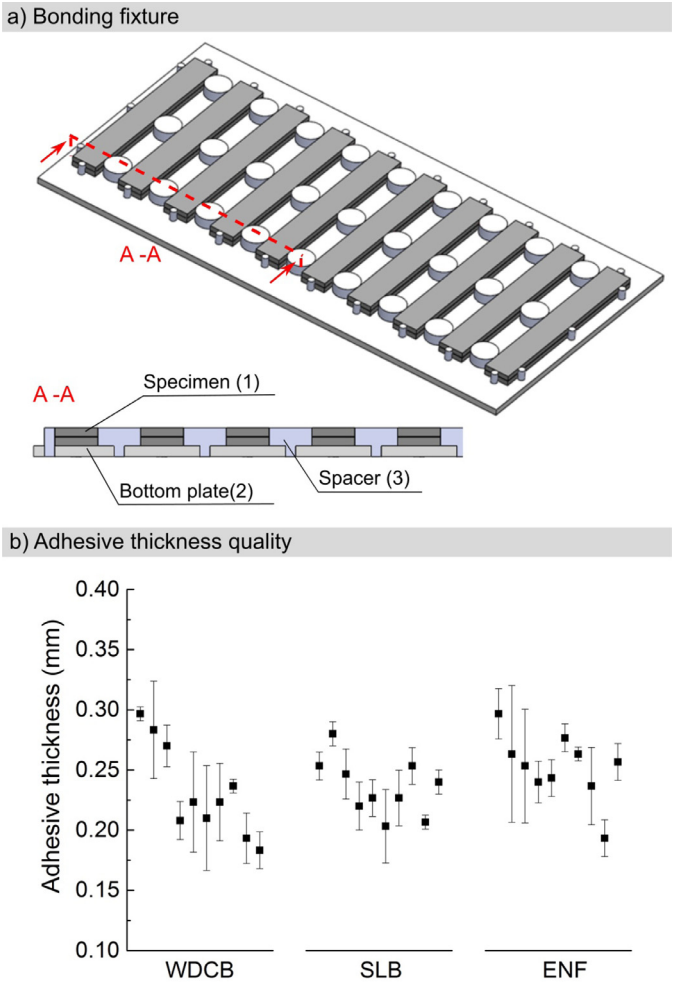

Fig. 2. a) The bonding fixture used to manufacture the test specimens and b) the bondline thickness values obtained for the different test specimens. (Nominal values was 0.25 mm).

with the end notched flexure (ENF) specimen, while a combination of both modes (I/II) was investigated using the single leg beam (SLB) specimen. The optimum specimen dimensions have been determined to ensure the specimens ability to reveal the mechanical performance of the adhesive interface under Split Hopkinson Bar loading without interference in the form of plastic deformation of the adherents. Hence, the beam length is $L = 146$ mm, the width is $b = 20$ mm and the height is $h = 4$mm. Considering the relationship [50]

$$a_{0,cr} = 0.35 \cdot L \tag{17}$$

the critical initial crack length for stable crack propagation is $a_{0,cr} = 23.8$ mm. Therefore, the initial crack length for the WDCB specimens are defined as $a_0 = 30$ mm, while for ENF and SLB specimens it is $a_0 = 34$ mm. The dimensions for each specimen configuration are shown in Fig. 1(b).

3.2. Specimen manufacturing and preparation

Fig. 2 (a) shows a custom made bonding fixture which was designed to accurately manufacture the specimens. Spacers were used to obtain the desired interface thickness. Bonding requires the activation of the adherent's surface to obtain optimal properties. Thus, the to-be-bonded surfaces were grit-blasted, cleaned and anodised following the procedure described elsewhere [51]. To introduce the crack length, a 12.0 μm thick Teflon sheet was introduced between two layers of film adhesive. The measured interface thickness of the manufactured specimens is reported for each fracture mode in Fig. 2(b). A deviation of 2.3%, 2.3% and 1.6% for the WDCB, ENF and SLB specimens from the nominal adhesive thickness of $t_a = 0.25$ mm was observed.

3.3. Experimental setup

The quasi-static (QS) and high-rate (HR) experiments were performed in laboratory conditions. A screw-driven Zwick machine was employed to load the specimens quasi-statically with a constant crosshead velocity of $v = 1$ mm/min. The load-displacement ($F - u$) curve was recorded during the experiment. A standard camera recorded images of the tested specimen at a speed of two frames per second at a resolution of 1546 x 2152 pixels. A fine gray-scale speckle pattern was applied to the surface of the specimen to monitor the crack length using digital image correlation (DIC). The initial crack length was marked with a ruler as it is shown in Fig. 3. The HR experiments were carried out using a Split Hopkinson Pressure Bar (SHPB) to subject the specimen to a velocity of $v = 4$ m/s. The SHPB setup for WDCB, ENF and SLB are different. While the setup for the WDCB specimens consists traditionally of an input and output bar and a striker, the output bar in the setup for ENF and SLB specimens is replaced with an in-house-made fixture holding the specimen in place – see Fig. 3. The diameter of the input and output bars is $d = 16$mm, while the length of the bars was $L_b = 2500$ mm. The striker had a length of $L_s = 2700$ mm with the same diameter as the input and output bars. Fig. 4 shows the dimensions and the setup of the used SHPB. Images were recorded using two high-speed cameras: a Photron camera recorded the displacement of the loading wedge/ pin with 150,000 frames per second and a resolution of 716 x 624 pixels, while a Special imaging Kirana camera monitored the crack length growth at 200,000 frames per second with a resolution 924 x 768 pixels.

For both loading regimes, the supports and loading pin for the ENF and SLB experiments are manufactured with a rounded tip and a radius of $r = 2.5$ mm. The wedge for the WDCB experiments is designed so that a sharp tip with an angle of $\alpha = 30^{\circ}$ is achieved. The bars and striker were made out of titanium alloy Ti–6Al–4V while the supports were made out of stainless steel. Table 1 summarises the mechanical properties for the two alloys. Fig. 3 summarises the difference in the setup for each specimen configuration.

One should note that in the present work, the SHPB is used exclusively to apply the dynamic deformation load at the fracture mechanics experiments – SHPB analysis theory was not employed. Due to the large scale of the experiments – which introduce geometric and material impedance mismatch, or inhomogeneous stress distribution – the authors believe that the readings from the strain gauges will not offer the most accurate representation of the mechanical behaviour. Therefore, a new data acquisition method has been developed which relies entirely on digital image correlation. This new method is explained in the following sub-section.

3.4. Data acquisition method

For calculating the fracture energy, one needs to measure the force and the crack length propagation during the failure process. Generally, the force-displacement curves obtained using standard equipment – *i.e.* testing machine output and DIC – are sufficient to obtain the J value. The CBBM method can be applied to the quasi-static ENF and SLB experiment data. However, the quasi-static force recordings of the WDCB specimens are influenced by the friction between the wedge and the adherents: a transformation of the force in its perpendicular components – the actual opening force – would need to consider those frictional effects. This introduces some uncertainties that would influence the accuracy of the results. Additionally, high-rate force readings obtained from strain gauge signals may not be accurate due to oscillations and inertia effects encountered during loading. The measured forces would require smoothing and filtering – this may masks the true

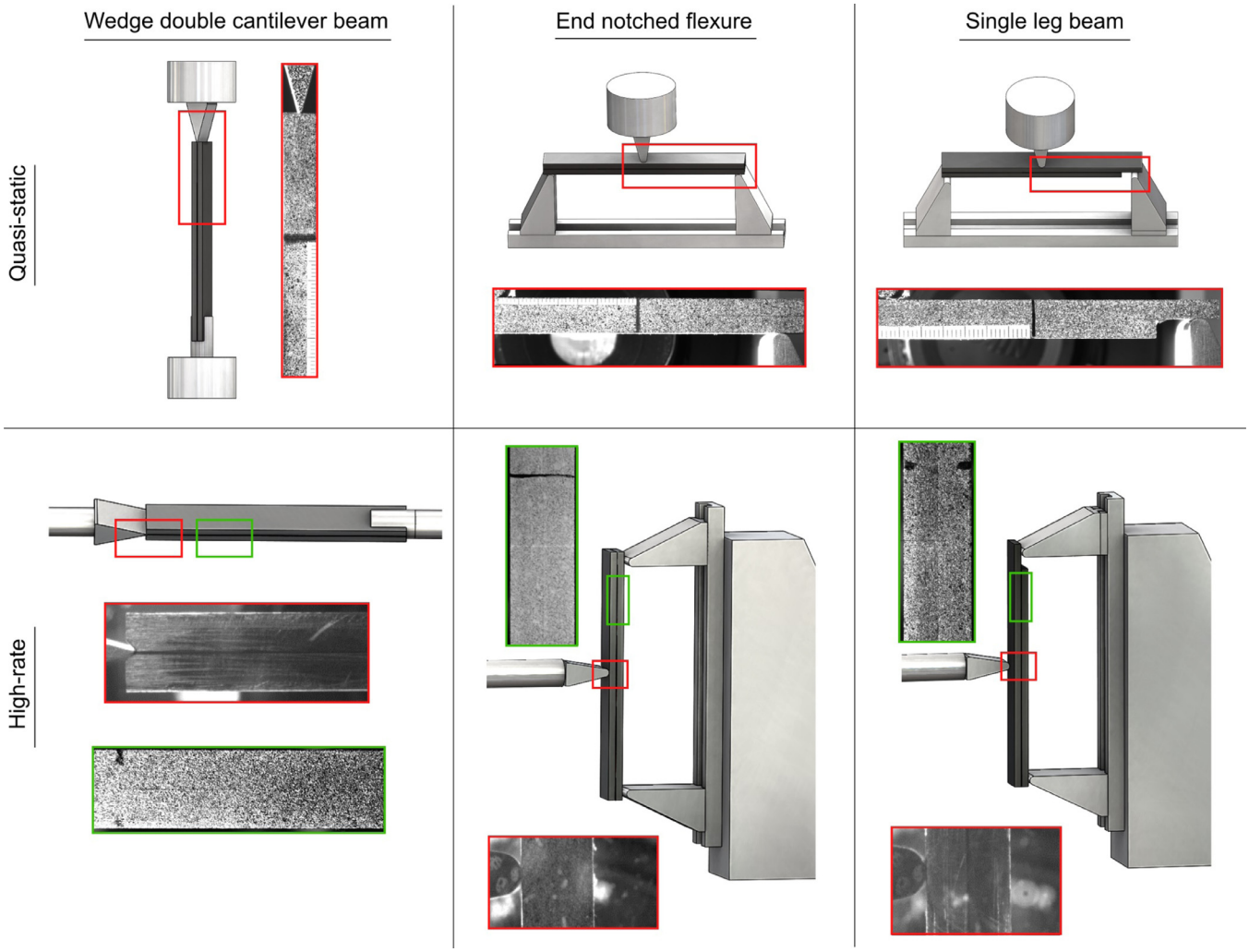

Fig. 3. Quasi-static and high-rate experimental setups for the three different fracture specimens WDCB, ENF and SLB.

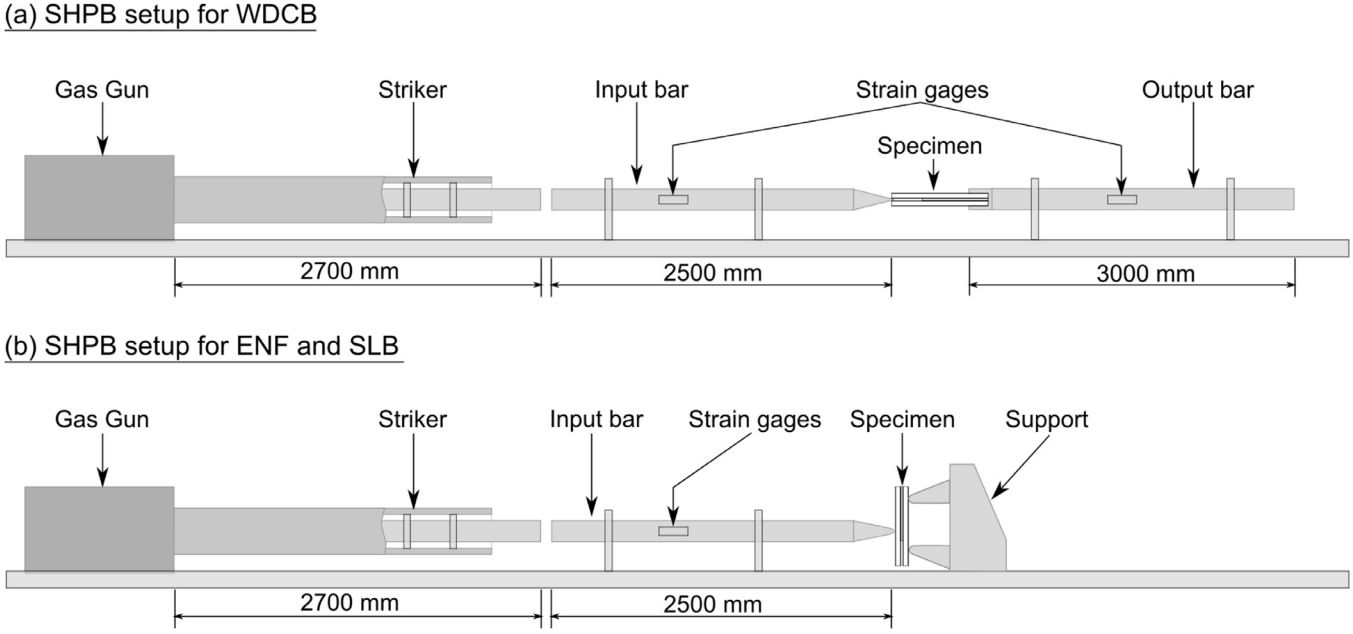

Fig. 4. Schematics of the SHPB setup for (a) WDCB specimens and (b) ENF and SLB specimens.

Table 1
Material properties of adherents, bars, striker and supports.

Metal	E (GPa)	ρ (g/cm^3)	ν	σ_y (MPa)
Ti–6Al–4V	114	4.43	0.34	900
Steel	200	8	0.29	-

mechanical performance of the joint. To overcome these limitations, a new measurement technique was developed. This technique overcomes the aforementioned challenges by exclusively relying upon digital image correlation (DIC). Fig. 5 illustrates the newly developed measurement technique. The method is described in the following paragraph.

The force F was calculated using the applied displacement u and the compliance C of the adherents using Eq. (4). The calculation of the compliance requires the crack length a – or a sufficiently high-resolution image. Therefore, this novel method relies upon measuring the applied displacement and the crack length using DIC. Firstly, a measurement position, which is represented as a red dot in Fig. 5, is selected. Using this, the displacement is obtained as a function of the time. Secondly, the crack length is estimated. A region of interest (ROI) is defined which includes the initial crack length. These are shown as black lines in Fig. 5. Thirdly, the stored displacement histories are then used to indicate the crack length propagation for each time step. For that, two points in the x-direction (which is aligned to the specimen width) are employed. These points are positioned on each substrate close to the adhesive interface. The sets of points act as virtual gauges which are used to obtain the opening displacement in the x-direction Δu (for WDCB) and in the y-direction Δv (for ENF and SLB) for each point-position. For ductile materials, a threshold is required to define the opening displacement in order to consider the influence of the FPZ. This can be obtained by measuring the opening displacement of the first crack propagation increment which is visible using the displacement field in the image analysis. The following relationship is defined to identify when displacements are larger than the threshold at the nth position:

$$\Delta u_{(y=y_n)_{(t=t_s)}} \geq \Delta u_{Threshold} \quad \text{and} \quad \Delta v_{(y=y_n)_{(t=t_s)}} \geq \Delta v_{Threshold}. \tag{18}$$

When the threshold is reached, the distance of y_n can be used to derive the crack length a at time t_s following

$$a_{t=t_s} = a_0 + y_{n_{(t=t_s)}} \quad . \tag{19}$$

By deriving the crack length as a function of time, the compliance of the joint can be calculated. Table 2 summarises the employed equations and measurement techniques for each loading regime separately. Using the new data acquisition method to obtain the compliance, the applied force is then calculated considering Eq. (4). Thus, the force-displacement behaviour and the fracture energy-crack length relationship are fully described.

4. Experimental results

This section quantifies and discusses the rate- and mode-dependent behaviour of adhesively bonded structures. First, the new experimental methodology is verified by comparing different measurement techniques. Second, the mechanical behaviour – as measured by the novel experimentation – of the adhesively bonded structures is presented. Third, fractography is used to isolate the nature of the fracture mode.

4.1. Verification of the new data acquisition method

Before the new measurement technique can be applied, it is necessary to verify its accuracy. This will add confidence to the obtained results. For this purpose, a verification process is proposed in Fig. 6. This will measure the precision of the generated quasi-static and high-rate experimental results. The verification process employs the force-displacement results of an ENF experiment. In a standard fashion, the force is obtained from the testing machine readings while the displacement is measured *via* DIC – these will be used as the benchmark. If the force-displacement readings generated with the new method match these benchmarks, the newly developed measurement technique is assumed verified and therefore valid for the measurement of both quasi-static and dynamic loading regimes.

However, these standard equations – which were developed for quasi-static loading conditions based on the simple beam theory (SBT) – need also to be proven in a high-rate loading regime. This is accomplished by focusing on the deflection of an adherent arm and by the determination of characteristic times. The compliance of one adherent arm of a WDCB experiment is calculated both for the quasi-static and the dynamic loading case – see Fig. 7. When a match between both loading regimes is achieved, one can assume that the equations derived from QS equilibrium are valid for high-rate analysis.

For the experiments one needs to calculate the characteristic times of the structures explained in detail by Delvare *et al.* [52]. These characteristics times can be defined as: (i) reference time, T_R, (ii) characteristic time, T_T and (iii) support reaction time, T_C. T_R is the effective duration of the test and corresponds to the elapsed time when the incident wave reaches the specimen and the fracture of the specimen. T_T represents the first response of the beam – which is defined by the duration of a round trip of the elastic wave, c, across the width of the specimen h, following

$$T_T = \frac{2h + t_a}{c} \tag{20}$$

where t_a is the thickness of the adhesive. Finally, T_C is related to the duration of the wave travelling from the impact location to the end of the specimen and back – this is described following

$$T_C = \frac{L}{c} \quad . \tag{21}$$

where L is the characteristic length of the specimen.

With a rough estimation of the characteristic times, it is possible to identify whether the experiments are in equilibrium. If it can be assumed that the specimens are in a dynamic equilibrium, the standard equations in Section 2 and summarised in Table 2 are applicable. This would mean that the supports are aware of each other's existence and that the force of the impactor (loading pin) is twice the force of the supports.

ENF experiments performed under QS conditions are analysed using the standard and the new measuring technique. Fig. 7(a) compares the force-displacement results recorded directly from the testing apparatus against the force-displacement extracted using DIC exclusively. Both force-displacement curves are in excellent agreement and shows the ability of the new method to capture the failure point with precision. This verifies the new method for high-rate experiments – if one assumes that the elastic deformation of the adherents is rate independent. This is supported by Fig. 7(b), which shows that the adherents' compliance of a WDCB specimen is rate independent: the deflection of one beam in QS (black lines) and HR (blue lines) are obtained and compared with each other. No major deviation is observed. Additionally, the characteristic times reveal that the reference time ($T_R = 500\,\mu s$) is large enough when compared to T_T and T_C (1.46 μs and 23 μs respectively). Therefore, one may consider that the HR experiments exhibit a dynamic equilibrium, thus allowing the use of the standard equations for calculating the necessary fracture parameters.

4.2. Experimental results: WDCB, ENF, and SLB

The results for the three investigated deformation modes experimented under QS and HR are summarised in Fig. 8. The quasi-static force results for the WDCB experiments have a mean fracture force of F

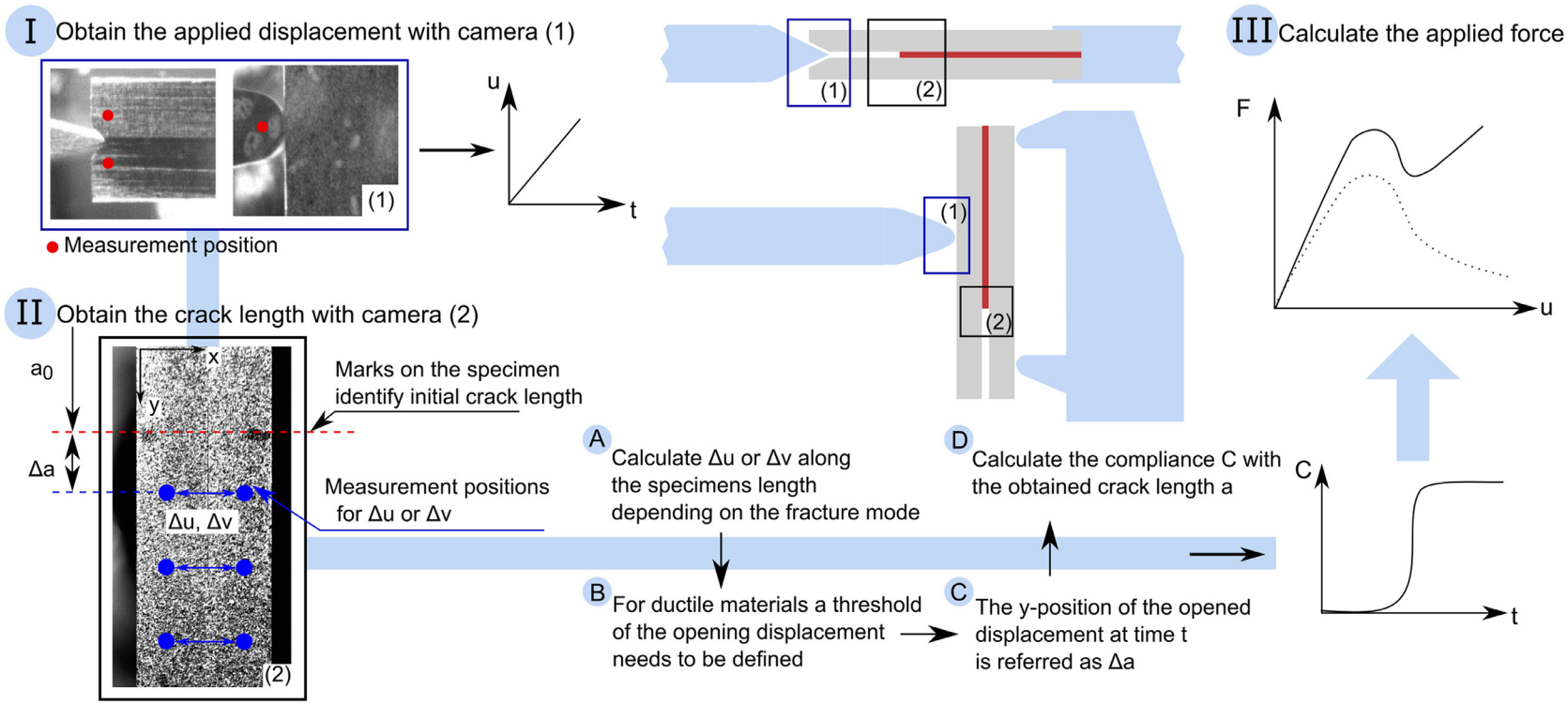

Fig. 5. The strategy shows the calculation of the force-displacement curve using a new measurement technique relying entirely on DIC.

Table 2
Overview of the employed equations for the calculation of the fracture energy in QS and HR loading regimes.

Equations for analysis	Wedge double cantilever beam (WDCB)	End notched flexure (ENF)	Single leg beam (SLB)
Compliance	$C(a) = \frac{8a^3}{Ebh^3} + \frac{12a}{5bhG}$	$C(a) = \frac{3a^3 + 2L^3}{8bh^3E} + \frac{3L}{10bhG}$ $C_c = C - \frac{3L}{10bhG}$ *and* $C_{0c} = C_0 - \frac{3L}{10bhG}$	$C = \frac{F}{u}$
Energy release rate	$J_{Ic}(a, F) = \frac{12a^2}{Eh^3b^2}F^2 + \frac{F}{b}(w_1' - w_2')\,w_1' - w_2'$ have been calculated following the procedure described in [49]	$J_{IIc}(a_e, F) = \frac{9F^2a_e^2}{16b^2h^3E_f}$ with $E_f = \frac{3a_0^3 + 2L^3}{8bh^3}\left(C_0 - \frac{3L}{10bhG}\right)^{-1}$	$J_{I/IIc}(a, F) = \frac{21F^2a^2}{16E_f b^2h^3} + \frac{3F^2}{10Gb^2h}$ $J_{Ic}(a, F) = \frac{12F^2a^2}{16E_f b^2h^3} + \frac{3F^2}{10Gb^2h}$ $J_{IIc}(a, F) = \frac{9F^2a^2}{16E_f b^2h^3}$ with $E_f = \frac{28a_0^3 + L^3}{32bh^3}\left(C_0 - \frac{3(a_0 + L)}{20bhG}\right)^{-1}$
		Quasi-static	
Crack length	Obtained with new measuring technique based on DIC using high-speed SI Kirana camera images	$a_e = \left[\frac{C_c}{C_{0c}}a_0^3 + \frac{2}{3}\left(\frac{C_c}{C_{0c}} - 1\right)L^3\right]^{\frac{1}{3}}$	Transform cubic equation to obtain the crack length a $C(a) = \frac{28a^3 + L^3}{32Ebh^3} + \frac{3(a + L)}{20Gbh}$
Displacement Force	$F(u) = \frac{u}{C}$	DIC or testing machine output	Testing machine output
		High-rate	
Crack length Displacement Force	Obtained with new measuring technique based on DIC using high-speed SI Kirana camera images Obtained with DIC using high-speed Photron camera images $F(u) = \frac{u}{C}$		

$= 983$ N with a standard deviation of $s = 6.8\%$. On the other hand, the QS ENF experiments result in a mean fracture force of $F = 4018$ N with a standard deviation of $s = 6.6\%$. For the same loading regime, the SLB experiments show a mean fracture force of $F = 2071$ with $s = 8.2\%$. As expected the mixed-mode experimental results represented by SLB specimens are larger than the mode I values (represented by WDCB specimens) but smaller than the mode II results (represented by the ENF specimens).

Accordingly, HR results of the WDCB experiments show a mean fracture force of $F = 540$ N with $s = 16.8\%$, while the ENF experiments result in a mean fracture force of $F = 2927.5$ N with $s = 13.4\%$. Also, the HR SLB experiment values of $F = 1486$ N and $s = 7.9\%$ are larger than the HR WDCB ones but smaller than the HR ENF values. The standard deviation up to $s = 16\%$ can be explained with the composition of the adhesive interface. Voids and imperfections within the adhesive interface are believed to cause scatter in mechanical performance. A negative rate-dependency of the force-displacement curves follow previous observations: the dissipated energy of the adhesive tends to decrease with an increase of deformation rate.

4.3. Rate-dependent fracture energy

This subsection quantifies the fracture energy, J, as a function of the different fracture modes and loading rates.

Employing Eqs. (13), (14), (15), and (16), the fracture energy for each deformation mode and loading regime is calculated and presented in Figure 9. HR fracture energies for each different deformation mode are lower than the obtained values in the QS regime. The relevant values of fracture energy and standard deviations are summarised in Table 3. It is shown that the QS measured fracture energies are within the trend of the results investigated by Alvarez [51] using similar methods. One should note that the results from [51] were obtained using different adhesive thicknesses and specimen geometries than the current study. Nevertheless, there is a close agreement between them. Moreover, Fig. 10 also compares the measured values of this study against those measured by the authors using butt joint, single lap joint and scarf joint experiments [15]. The difference between these characterisation experiments and the fracture mechanics experiments are rationalised in a later section.

Finally, a rate dependent failure envelope using the measured fracture energies is generated and presented in Fig. 11. Based on the Benzeggagh-Kenan (BK) and power law criterion, the relationship between the modes of failure can be obtained for both QS and HR regimes. This failure envelope enables design engineers to interpolate the measured fracture behaviour in the most appropriate loading conditions.

4.4. Fractography analysis: on the nature of failure

In order to assure that the measured fracture energies belong to the adhesive interface, it was necessary to study in detail the fracture surface of the tested specimens. Thus, the fractured surfaces of representative specimens were investigated with a 3D optical microscope (Alicona). The profilometer allows one to reconstruct three-dimensionally and with great precision the fracture surface of the samples. Fig. 12 shows optical micrographs for each deformation mode and loading rate. Moreover, the profile height of each surface was measured in order to determine whether cohesive failure within the adhesive interface or adhesion failure at the interface between adherent and adhesive occurred. The profile lines presented in Fig. 12 show average heights of approximately 0.15 to 0.20 mm. Given that the adhesive measures approximately 0.25 mm in thickness, it is reasonable to believe that cohesive failure is dominant. The optical micrographs also reveal the presence of adhesive at both sides of the specimen. Moreover, optical analysis also reveals the existence of voids and carrier fibres. These have been considered previously [15] as important features that contribute to the failure behaviour of the adhesive interface. Finally, the higher fracture energy observed in ENF specimens is believed due to multiple micro-crack creation ahead the crack tip, subsequent coalescence, and increase in friction of the surfaces resulting in additional energy absorption.

5. Numerical method

One of the objectives of the present work is to employ fracture mechanics experiments to validate a cohesive zone model (CZM) – which was calibrated using butt joint, single lap joint and scarf joint experiments [15] (also named characterisation experiments from here onwards). Models of this kind are often used in finite element analysis

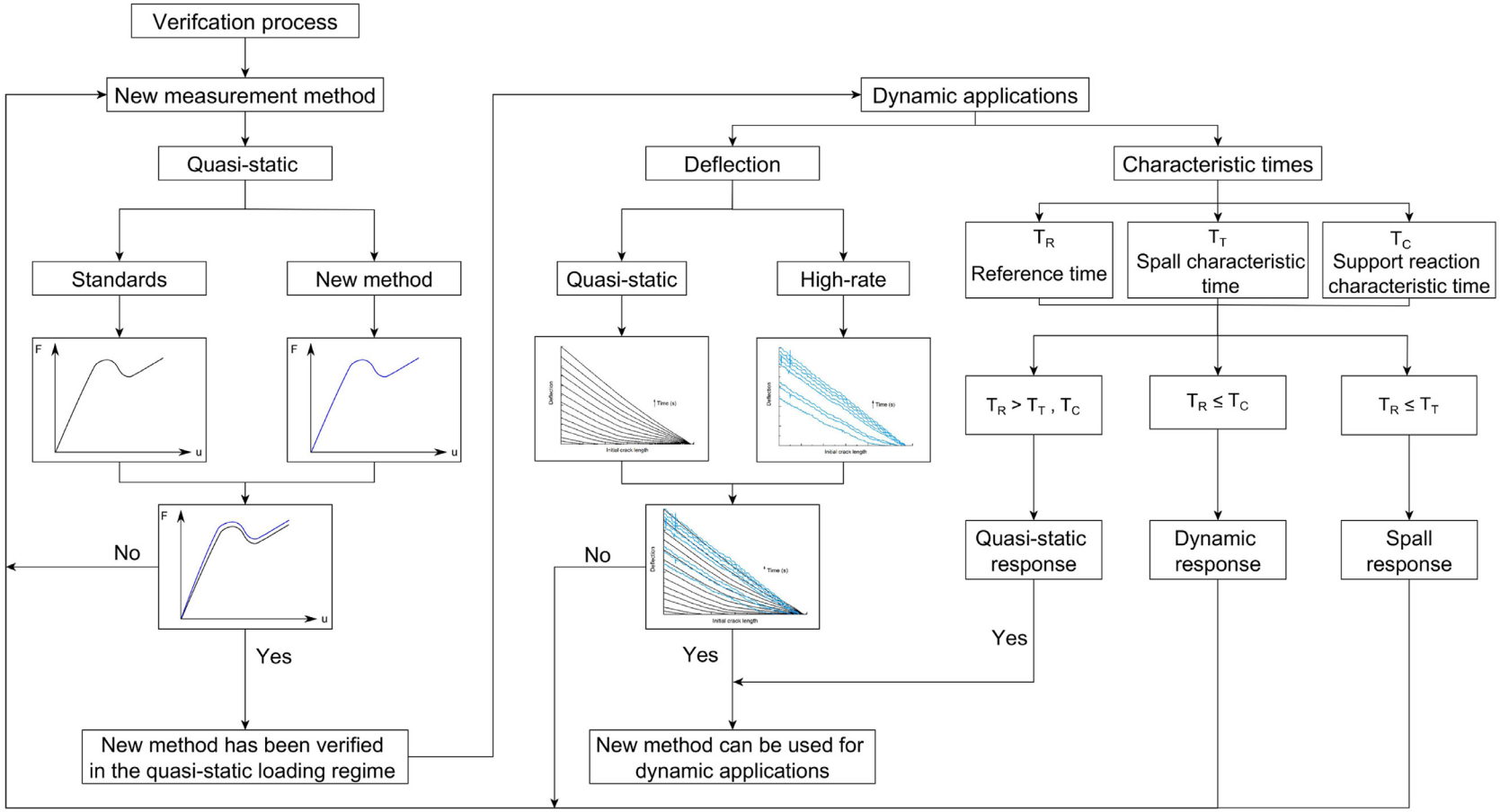

Fig. 6. The new measurement technique is verified for the quasi-static and dynamic loading regime following this verification process.

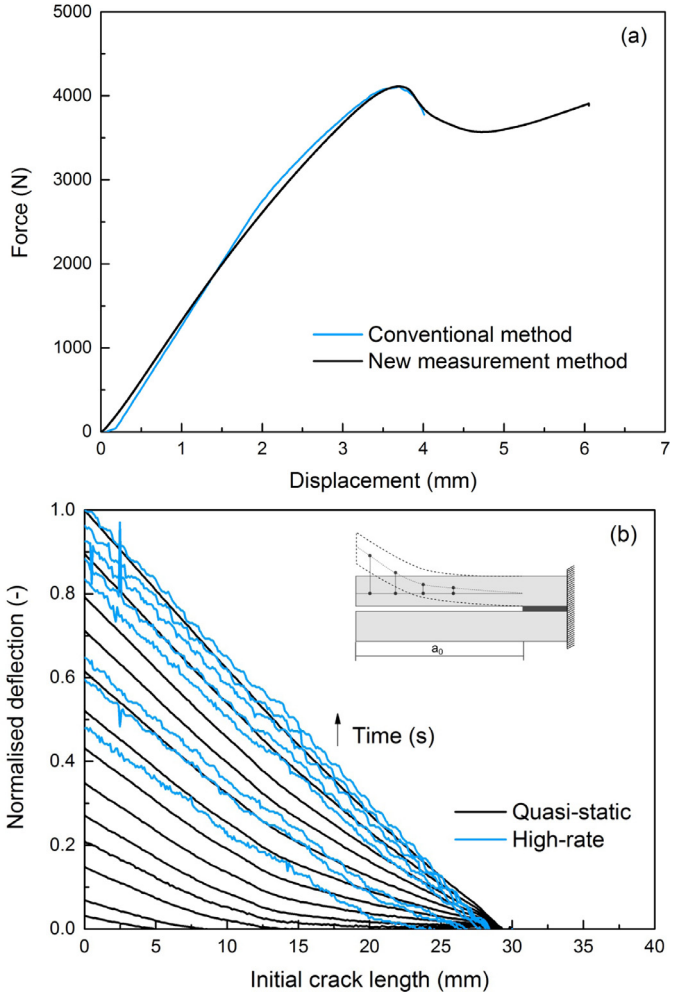

Fig. 7. The new measurement technique is verified by a) the comparison of experimental ENF results calculated using standard and new method and b) the quasi-static and high-rate deflection results of a WDCB specimen.

to simulate and predict the behaviour of complex adhesively bonded structures. Fig. 13 demonstrates the process which has been followed to prove the models ability to predict failure. This section also details the setup of the finite element models developed for the WDCB, ENF, and SLB experiments (also named fracture mechanics experiments from here onwards). The behaviour of the adhesive employed has been previously measured and modelled in the form of a CZM in previous work from the authors. The CZM is summarised next.

5.1. Material model

The CZM developed allows the modelling of a rate, thickness, and deformation mode dependent traction separation law (TSL) for adhesive interfaces following a trapezoidal shape. Fig. 13 shows the used nomenclature for representing the model. The plateau area represents plastic deformation caused by crack initiation, crack nucleation and crack coalescences. The whole area under the TSL curve is presented by the dissipated energy. The model characteristic rate-dependent parameters are explained next.

The rate dependent peak stress for the mode I and mode II contributions are implemented following a logarithmic function expressed as

$$T_N(\dot{\varepsilon}_N, f_v) = \left[T_{refN} + T_{0N}\cdot\ln\left(\frac{\dot{\varepsilon}_N}{\dot{\varepsilon}_{ref}}\right)\right]\cdot(1 - f_v) \tag{22}$$

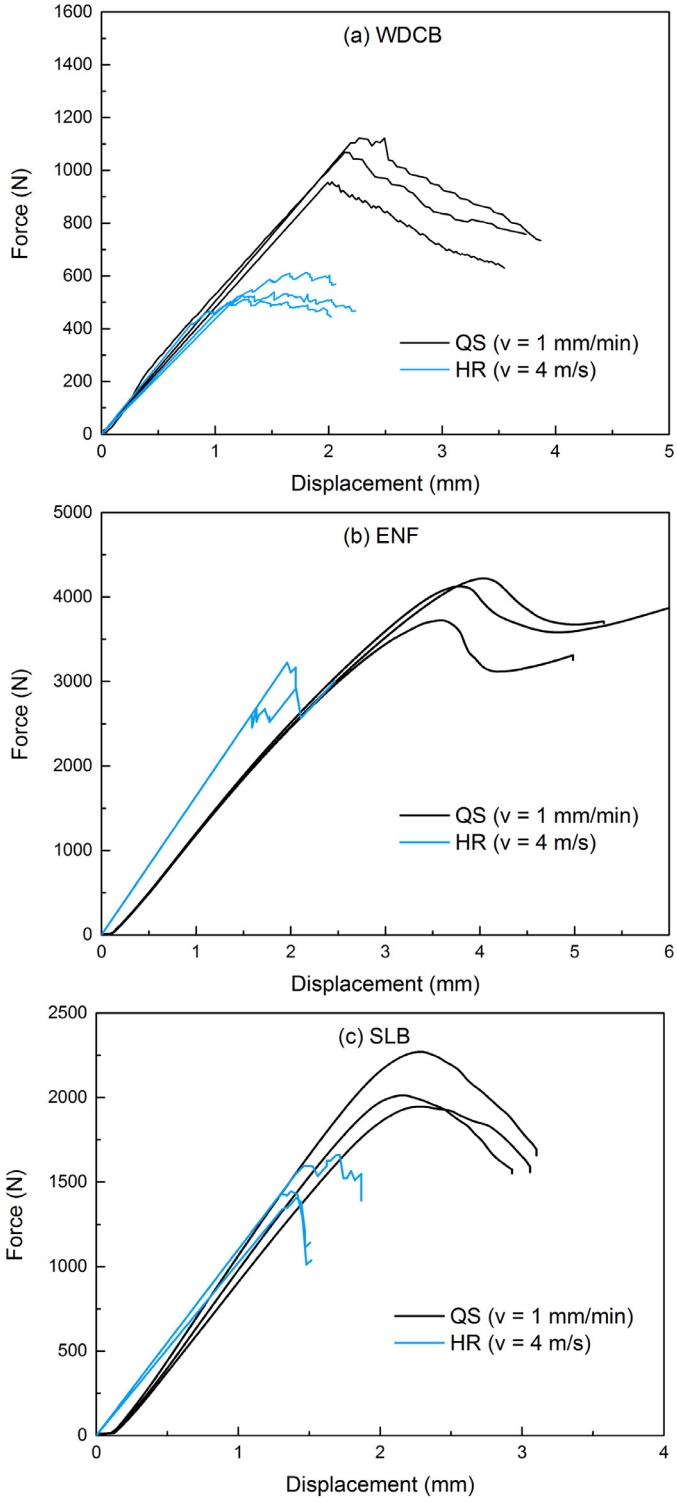

Fig. 8. Rate-dependent force-displacement results for the three investigated fracture modes: a) WDCB, b) ENF and c) SLB.

and

$$T_S(\dot{\varepsilon}_S, f_v) = \left[T_{refS} + T_{0S}\cdot\ln\left(\frac{\dot{\varepsilon}_S}{\dot{\varepsilon}_{ref}}\right)\right]\cdot(1 - f_v) \tag{23}$$

where, T_{refN}, T_{refS} and T_{0N}, T_{0S} are the reference values of peak stress and the strain rate sensitivity parameters respectively. The parameter $\dot{\varepsilon}_{ref}$ is the reference strain rate, and $\dot{\varepsilon}_i$ is the updated strain rate for $i = N, S$ which represent mode I and mode II respectively. The

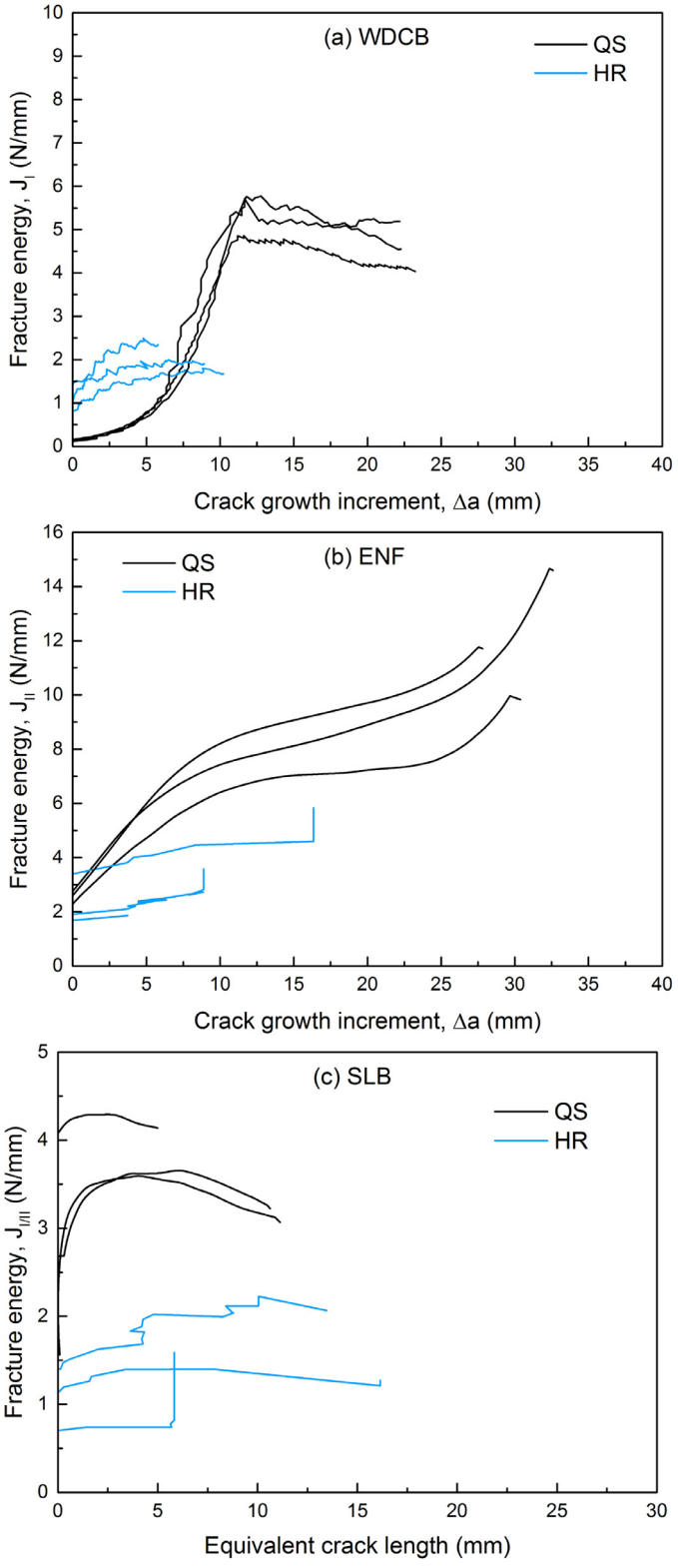

Fig. 9. Rate-dependent fracture energy-crack length results for the three investigated fracture modes: a) WDCB, b) ENF and c) SLB.

parameter f_v represents the void volume fraction which has been defined in previous studies [15] to be dependent on the adhesive interface thickness. It is expressed with

$$f_v(t_a) = f_{vref} \cdot t_a^{-f_{v0}} \tag{24}$$

where f_{vref} is the reference value and f_{v0} is the thickness sensitivity parameter.

Table 3
Mean value and standard deviation of the fracture energy, J (N/mm), for QS and HR regimes, and the three different fracture modes.

Rate	WDCB	ENF	SLB
QS	3.68 ± 0.53	8.40 ± 1.20	3.83 ± 0.40
HR	1.43 ± 0.25	4.50 ± 0.36	1.50 ± 0.26

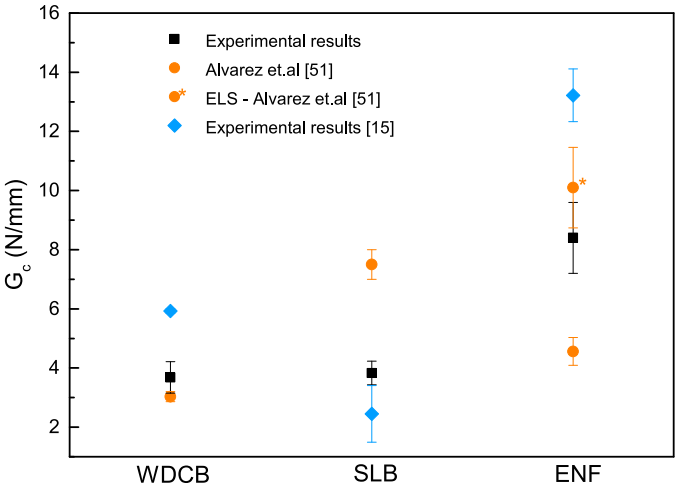

Fig. 10. Fracture energy (dissipated energy) comparison between results obtained in the present study and results found in the literature.

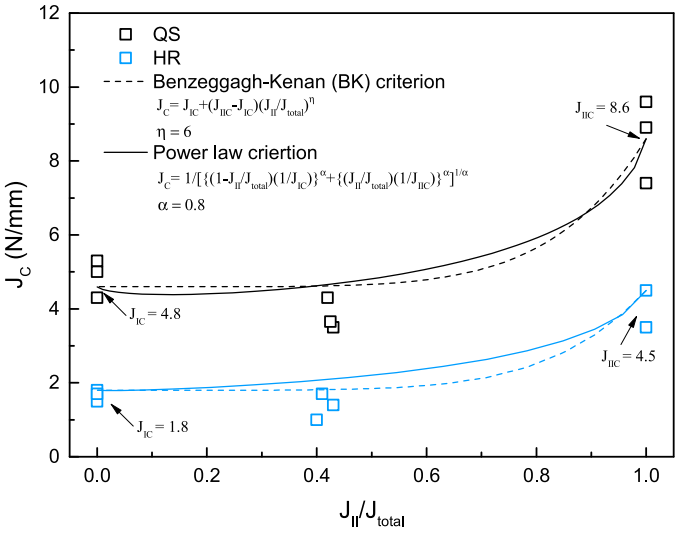

Fig. 11. The failure envelope of the AF 163-2OST adhesive interface using rate-dependent experiments of WDCB (mode I), ENF (mode II) and SLB (Mixed-mode).

Similarly, the dissipated energy (fracture energy) also follows a logarithmic function which can be written for mode I as

$$G_{cN}(\dot{\varepsilon}_N, f_v) = \left[G_{refN} - G_{0N} \cdot \ln\left(\frac{\dot{\varepsilon}_N}{\dot{\varepsilon}_{ref}}\right)\right] \cdot (1 - f_v) \cdot (1 - \frac{t_0}{t_a}) \tag{25}$$

while the mode II dissipated energy G_{cS} is described as:

$$G_{cS}(\dot{\varepsilon}_S, f_v) = \left[G_{refS} - G_{0S} \cdot \ln\left(\frac{\dot{\varepsilon}_S}{\dot{\varepsilon}_{ref}}\right)\right] \cdot (1 - f_v) \cdot (1 - \frac{t_0}{t_a}) \tag{26}$$

where G_{refN} and G_{refS} are the reference values of the dissipated energy in mode I and mode II respectively, and G_{0N} and G_{0S} represent the strain

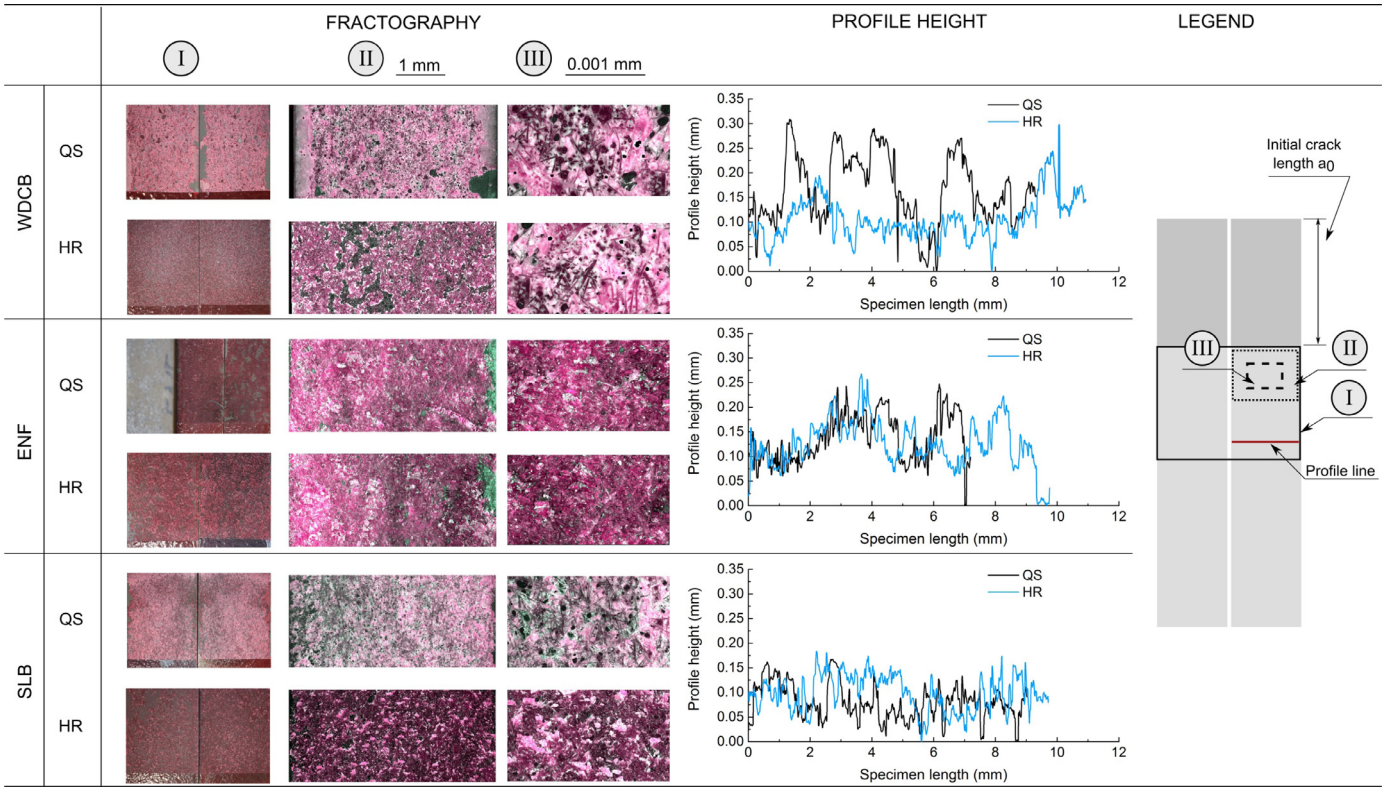

Fig. 12. Fractography of representative fracture surface for WDCB, ENF and SLB specimens investigated in quasi-static and high-rate loading conditions demonstrate cohesive failure of the specimens.

rate sensitivity parameters for each mode. The parameter t_0 describes the thickness reference value.

Since previous experimental observations suggest a rate dependent behaviour of the plateau area it is considered in the model. This was done by introducing a plateau ratio which represents the relationship between the plateau area and the dissipated energy. According to

$$P_N(\dot{\varepsilon}_N) = P_{refN} \cdot \left(\frac{\dot{\varepsilon}_N}{\dot{\varepsilon}_{ref}}\right)^{p_N} \tag{27}$$

and

$$P_S(\dot{\varepsilon}_S) = P_{refS} \cdot \left(\frac{\dot{\varepsilon}_S}{\dot{\varepsilon}_{ref}}\right)^{p_S} \tag{28}$$

the plateau ratios for mode I and II are described, respectively. The parameters P_{refN} and P_{refS} are the reference values for mode I and mode II respectively, and p_N and p_S are the strain rate sensitivity parameters of the plateau ratio.

In the following the shape given parameters for the CZM are explained: The mixed-mode behaviour of the TSL is defined by a quadratic criterion for the yielding initiation expressed as

$$\left(\frac{\delta_{m1,I}}{\delta_{n1}}\right)^2 + \left(\frac{\delta_{m1,II}}{\delta_{s1}}\right)^2 = 1, \tag{29}$$

while a linear criterion describes the damage initiation and final failure using the expression

$$\left(\frac{\delta_{mi,I}}{\delta_{ni}}\right) + \left(\frac{\delta_{mi,II}}{\delta_{si}}\right) = 1 \qquad i = 2, f \tag{30}$$

The yield initiation δ_{m1} can be calculated using the expression

$$\delta_{m1} = \delta_{n1}\delta_{s1}\sqrt{\frac{1+\beta^2}{\delta_{s1}^2 + (\delta_{n1}\beta)^2}} \tag{31}$$

considering an equivalent mixed-mode displacement

$$\delta_{m1} = \sqrt{\delta_{m1,I}^2 + \delta_{m1,II}^2} \tag{32}$$

and a mixed-mode ratio with

$$\beta = \frac{\delta_{m1,II}}{\delta_{m1,I}}. \tag{33}$$

The yield initiation displacement is then fully described with the relevant displacements for each mode separately. This is described following

$$\delta_{n1} = \frac{T_N}{K_n} \quad \text{and} \quad \delta_{s1} = \frac{T_S}{K_s} \tag{34}$$

where the indices n and s represent mode I and mode II respectively. The stiffness for each mode is calculated with

$$K_n = \frac{E}{t_{el}} \quad \text{and} \quad K_s = \frac{G}{t_{el}} \tag{35}$$

where E is the Young's modulus (2000 MPa) of the adhesive, G the shear modulus of the adhesive (220 MPa), and t_{el} the element thickness.

The damage initiation δ_{m2} and the final failure displacement δ_{mf} are described in a similar way using

$$\delta_{mi} = \delta_{ni}\delta_{si}\frac{\sqrt{1+\beta^2}}{(\beta\delta_{ni} + \delta_{si})} \qquad i = 2, f. \tag{36}$$

The relevant mode I and II dependent components for the damage initiation are described by

$$\delta_{n2} = \delta_{n1} + \frac{2 \cdot G_{cN} \cdot P_N}{T_N \cdot (1+\gamma_N)} \quad \text{and} \quad \delta_{s2} = \delta_{s1} + \frac{2 \cdot G_{cS} \cdot P_N}{T_S \cdot (1+\gamma_S)}. \tag{37}$$

while the mode I and II components for the final failure displacement are expressed as

$$\delta_{nf} = \delta_{n1} + \delta_{n2} + \frac{2 \cdot G_{cN}}{T_N \cdot \gamma_N} - \frac{\delta_{n2} + \gamma_N \cdot (\delta_{n2} - \delta_{n1})}{\gamma_N} \tag{38}$$

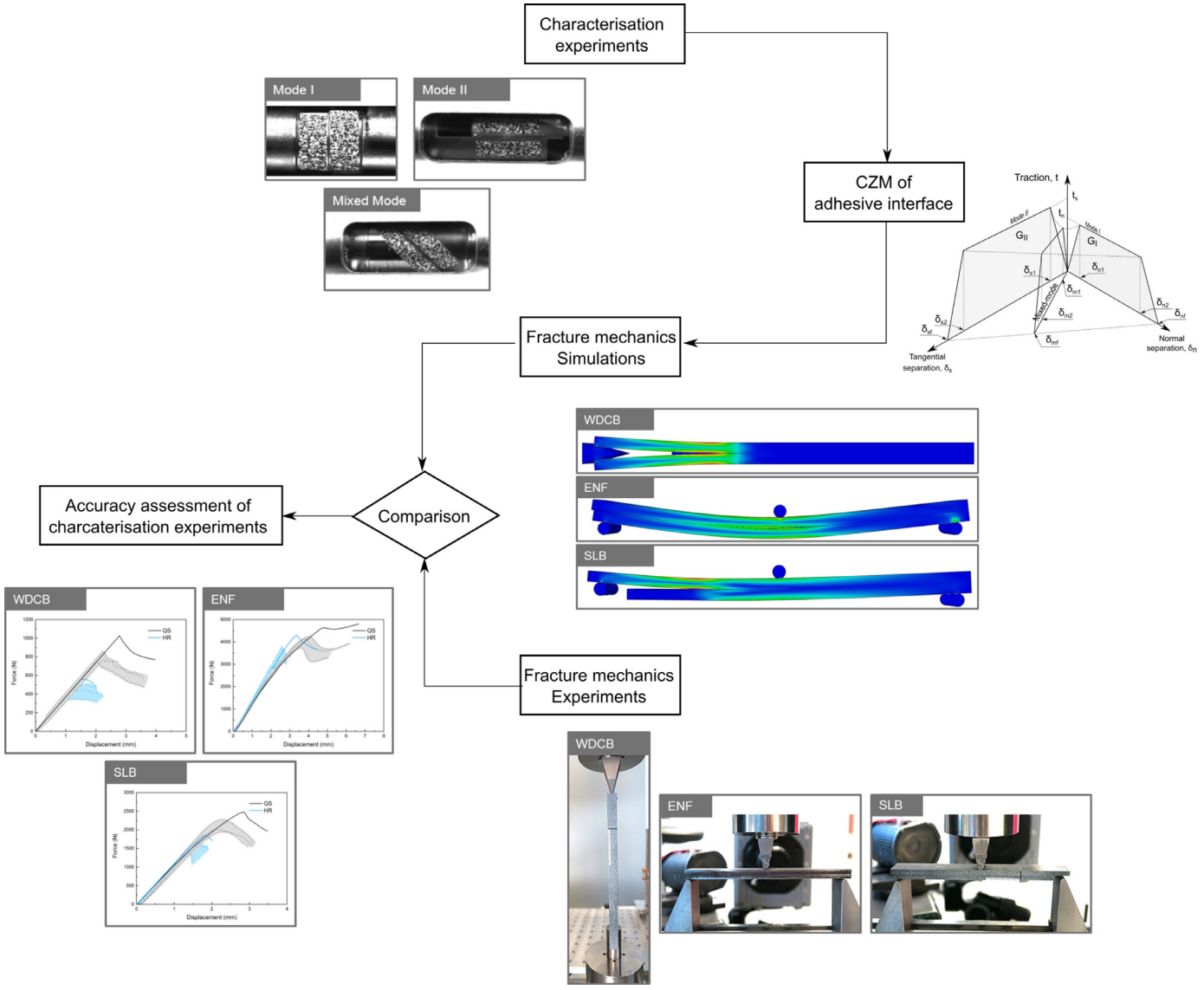

Fig. 13. Process for the accuracy assessment of the developed CZM.

and

$$\delta_{sf} = \delta_{s1} + \delta_{s2} + \frac{2 \cdot G_{cS}}{T_S \cdot \gamma_S} - \frac{\delta_{s2} + \gamma_S \cdot (\delta_{s2} - \delta_{s1})}{\gamma_S} \tag{39}$$

where the parameters γ_N and γ_S enable the representation of a softening plateau area. These parameters represent a fraction of the maximum traction decsribed by

$$t = (1 - d) K \delta. \tag{40}$$

Then, the damage d can be fully defined as

$$d = \begin{cases} 0, & \delta_m \le \delta_{\mathrm{m1}} \\ 1 - \dfrac{\delta_{m1}}{\delta_m} \cdot \left[1 + \dfrac{(\gamma_m - 1)(\delta_m - \delta_{m1})}{(\delta_{m2} - \delta_{m1})} \right], & \delta_{\mathrm{m1}} < \delta_m \le \delta_{\mathrm{m2}} \\ 1 - \left[\dfrac{\gamma_m \cdot \delta_{m1}}{\delta_m} \cdot \dfrac{(\delta_{mf} - \delta_m)}{(\delta_{mf} - \delta_{m2})} \right] \cdot & \delta_{\mathrm{m2}} < \delta_m \le \delta_{\mathrm{mf}} \\ \left[2 \cdot \left(\dfrac{\delta_m - \delta_{\mathrm{m2}}}{\delta_{\mathrm{mf}} - \delta_{\mathrm{m2}}} \right)^3 - 3 \cdot \right. & \\ \left. \left(\dfrac{\delta_m - \delta_{\mathrm{m2}}}{\delta_{\mathrm{mf}} - \delta_{\mathrm{m2}}} \right)^2 + 1 \right], & \\ 1, & \delta_m > \delta_f \end{cases} \tag{41}$$

where γ_{m} represents the percentage of plateau decrease for the mixed mode case and that follows

$$\gamma_{\mathrm{m}} = \sqrt{\frac{\gamma_{\mathrm{N}}^2 + (\beta \cdot \gamma_{\mathrm{S}})^2}{(1 + \beta^2)}}. \tag{42}$$

Consequently, the traction-separation relationship following Eq. 40 is fully described by considering that the stiffness K of the structure also includes the influence of mode I and mode II employing

Table 4
Material model properties for the AF 163-2OST adhesive.

E(MPa)	G(MPa)	T_{refN}(MPa)	T_{0N}	G_{refN}(N/mm)	G_{0N}	P_{refN}
2000	220	38.00	1.90	5.6	0.23	0.65
p_N	γ_N	T_{refS}(MPa)	T_{0S}	G_{refS}(N/mm)	G_{0S}	P_{refS}
-0.01	1.00	36.00	1.80	13.65	0.25	0.80
p_S	γ_S	f_{vref}	f_{v0}	t_0		
-0.03	0.85	0.54	0.02	0.038		

$$K = \sqrt{\frac{K_n^2 + (\beta \cdot K_s)^2}{(1+\beta^2)}} \tag{43}$$

The material parameters of the AF 163-2OST adhesive are summarised in Table 4.

5.2. Numerical setup

Simulations of the investigated deformation modes were performed to validate the CZM developed previously by the authors [15] and summarised above. In order to validate the CZM by comparing to the experiments, the same boundary and loading conditions must be applied. The simulations were carried out in 3D using the finite element solver Abaqus/Standard. C3D8 elements were used to discretise the adherents. The adhesive interface was modelled using 3D cohesive elements with 4 integration points by modelling the adhesive thickness geometrically. Each specimen configuration modelled follows the dimensions used in the experiments. The size of the elements for adherents and adhesive parts were 0.5 x 0.5 x 0.5 and 0.3 x 0.5 x 0.5 mm in thickness, width and length respectively. For the boundary conditions, the end of the WDCB specimen has been restricted in all the degrees of freedom (DOF). A friction coefficient of 0.1 was chosen between the wedge and the specimen arms. This was verified by comparing the experimental and numerically obtained wedge-force. Additionally, the ENF and SLB experiments were modelled with a friction coefficient of 0.1 between the specimen and the supports. The movement of the lower supports were restricted in all DOF while the loading pin was restricted in all DOF apart from the loading direction. The velocity was applied at the corresponding loading pin for the WDCB, ENF and SLB experimental setups. The simulation setups are summarised in Fig. 14.

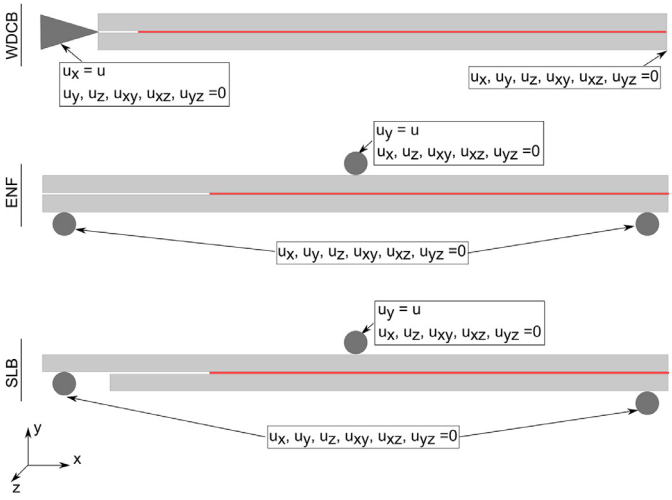

Fig. 14. The simulations for the WDCB, ENF and SLB experiments are constraint with the shown boundary conditions.

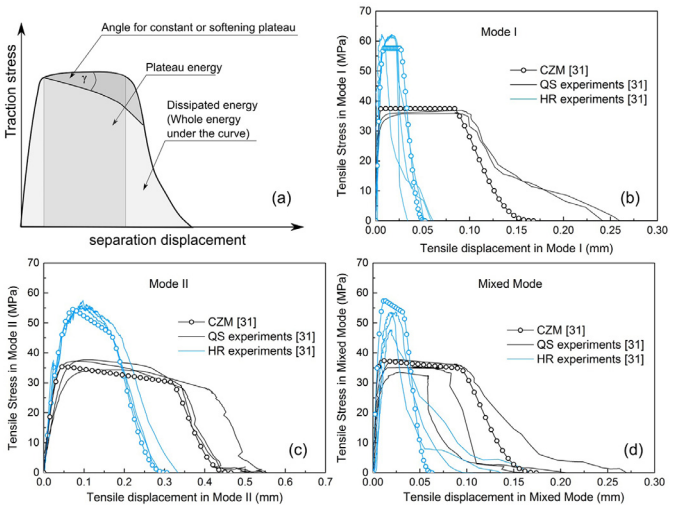

Fig. 15. Representation of (a) the used terminology, (b) TSL for Mode I, (c) TSL for Mode II and (d) TSL for Mixed Mode.

6. Numerical results

The traction-separation behaviour of the model is illustrated in Fig. 15 for different rates and loading modes. Both experimental results from previous characterisation experimentation [15] and CZM are shown. Our goal is to use the fracture mechanic results to validate the model. This validation process is critical, particularly when one intends to use their interpolation capacity. Here, we use the newly developed measuring technique to validate the adhesive CZM both under quasi-static and dynamic loading regimes.

Figs. 16, 17 and 18 compare the experimental and simulated behaviour of the WDCB, ENF, and SLB tests respectively. Simulations show good agreement to the experimental results – these are able to capture both the rate and the deformation mode dependence of the fracture process. No significant mesh size dependency on the numerical results was observed. Figs. 16–18 show the results for each fracture mode in 3D. Additionally, the graphs show the displacement field of experiments and models at different points during the fracture process – these are highlighted accordingly in the force-displacement curves. It is observed that the simulations slightly over-predict the experimental results. Nevertheless, it is reasonable to believe that both are in reasonable good agreement. The deviation between the simulation and the average experimental results in QS is 12.9%, 13.0% and 18.0% while in HR it is 20.0%, 18.0% and 16.0% for WDCB, ENF and SLB respectively. This over prediction can be explained when comparing the fracture energy values for the characterisation and fracture mechanics experiments in mode I and mode II loading. Fig. 19 shows that the model is overpredicting when comparing with the values of the fracture mechanics experiments.

In order to quantify this difference, some simple inverse modelling is carried out. It was found that lowering the reference values of the model dissipated energy greatly improves the agreement between models and fracture mechanics experiments. The value G_{refN}(N/mm) was reduced from 4.3 to 3 *N/mm* and the value for G_{refS}(S/mm) from 10.5 to 9 *N/mm*. Results are presented and compared in Fig. 19. Simulations with reduced reference energies result in an improved prediction of the experimentally obtained force-displacement curves for the WDCB, ENF and SLB experiments – these are shown in Fig. 20. These results prove that the characterisation experiments are able to accurately capture the peak traction of the adhesive. In terms of energy measurements, a difference between characterisation and fracture mechanics experiments between 10 and 20% is observed – depending on the loading mode.

This over-prediction of the energy by the characterisation

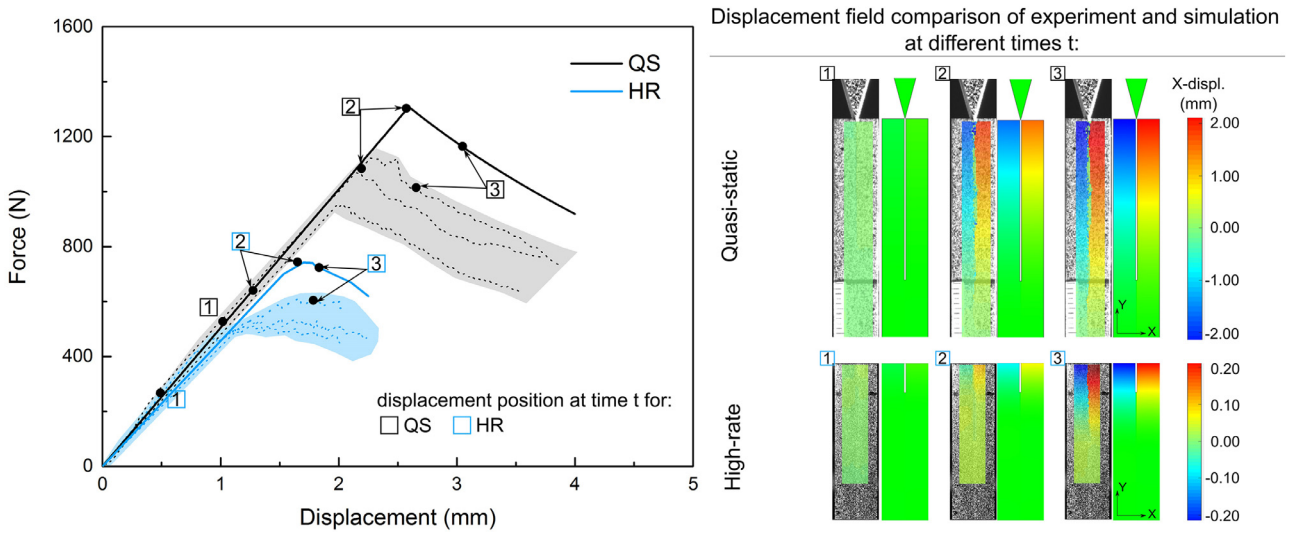

Fig. 16. Comparison of rate-dependent WDCB experimented and simulated force-displacement results. Different force-displacement positions in numerical model and experiments demonstrate a good representation of the experiments using the simulations.

experiments might be due to several reasons: (i) boundary edge effects exist in the characterisation experiments but not in the fracture mechanics experiments (due to the miniaturised nature of the characterisation experiments), (ii) small experimental measurement deviation in either of the experimental approaches, (iii) differences in thickness, (iv) differences in the surface specimen preparation, (v) different amounts of porosity, (vi) additional failure mechanisms such as fibre debonding or fibre pull-out which are not accounted for in the model or (vii) a combination of all of the above. Nevertheless, the discrepancies are small. Our results are useful in validating and improving the proposed cohesive zone model. The modelling work also helps in assessing and reinforcing the new measurement technique for dynamic fracture mechanics experiments. The technique outlined here provides a valid and comparatively simple approach to analyse high-rate deformation of adhesively bonded structures.

7. Conclusions

This work investigates the rate-dependence of fracture mechanics experiments in the form of the WDCB, ENF and SLB experiments by proposing a new measuring technique valid for both quasi-static and dynamic experimentation. These experiments impose mode I, mode II and mixed-mode I/II loading on the joint respectively. Experimental results are then used to validate a CZM of the adhesive interface. The following conclusions can be drawn from this work:

1. A novel measurement technique that can be used in dynamic environments is developed. This relies entirely upon DIC, thus circumventing any dynamic effect during experimentation. This method is successfully verified in the quasi-static and high-rate loading regimes by comparing directly to standard measuring techniques in QS and by comparing the compliance between QS and HR measurements.
2. This method is then used to measure the rate- and fracture-mode dependent mechanical properties of a structural adhesive interface under QS and HR regimes. Analysis reveals the maximum force and dissipated energy of the adhesive structures.
3. The experimental results for the three different modes of fracture mechanics experiments revealed a negative rate-dependent behaviour for the force-displacement curves – the fracture energy exhibited a decrease with increasing loading rate.
4. Fractography analysis showed that the adhesive fracture is

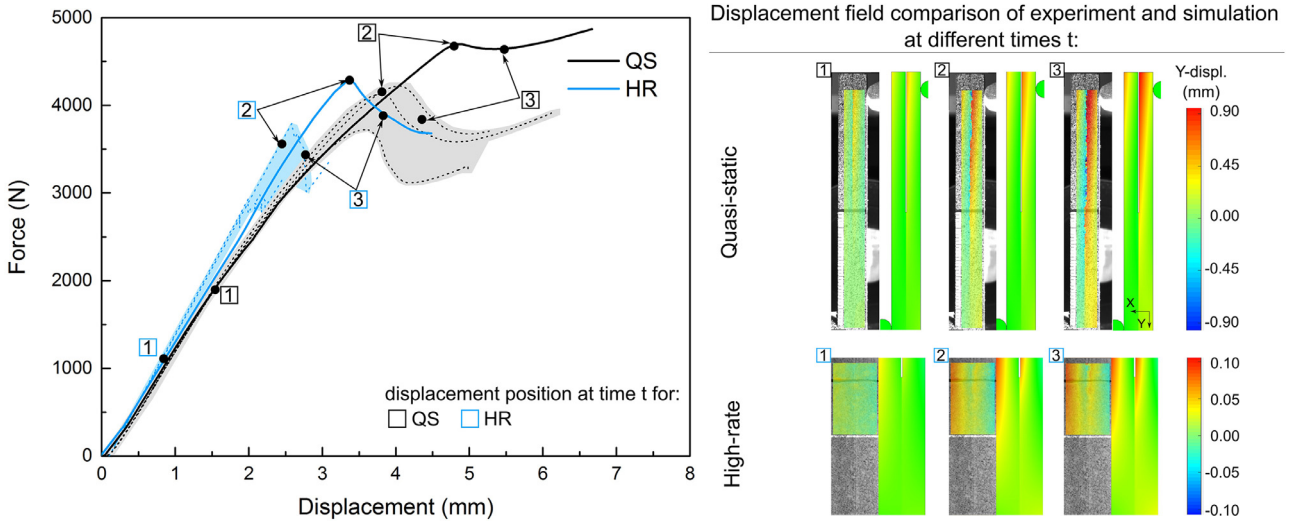

Fig. 17. Comparison of rate-dependent ENF experimented and simulated force-displacement results. Different force-displacement positions in numerical model and experiments demonstrate a good representation of the experiments using the simulations.

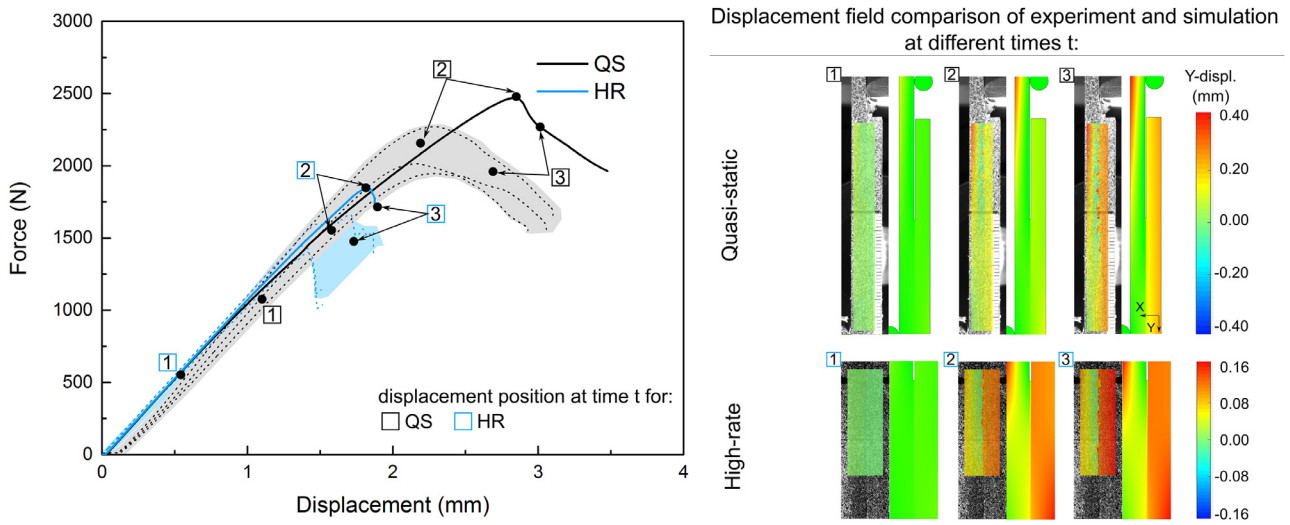

Fig. 18. Comparison of rate-dependent SLB experimented and simulated force-displacement results. Different force-displacement positions in numerical model and experiments demonstrate a good representation of the experiments using the simulations.

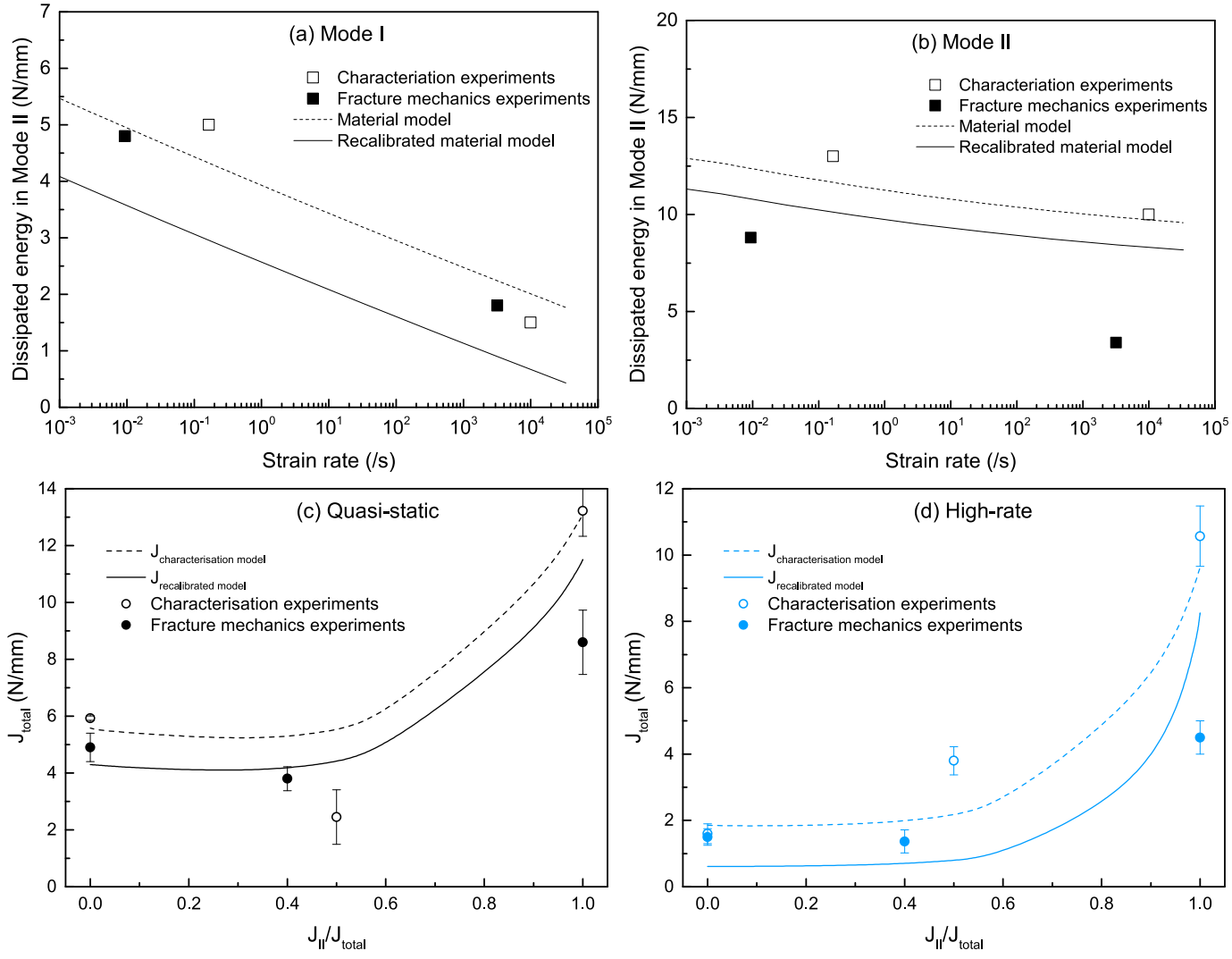

Fig. 19. Comparison of the absolute values of fracture energy for characterisation [15] and validation experiments and the material model for (a) mode I and (b) mode II loading and presentation of the recalibrated material model representation compared to the material model for (c) quasi-static and (d) high-rate.

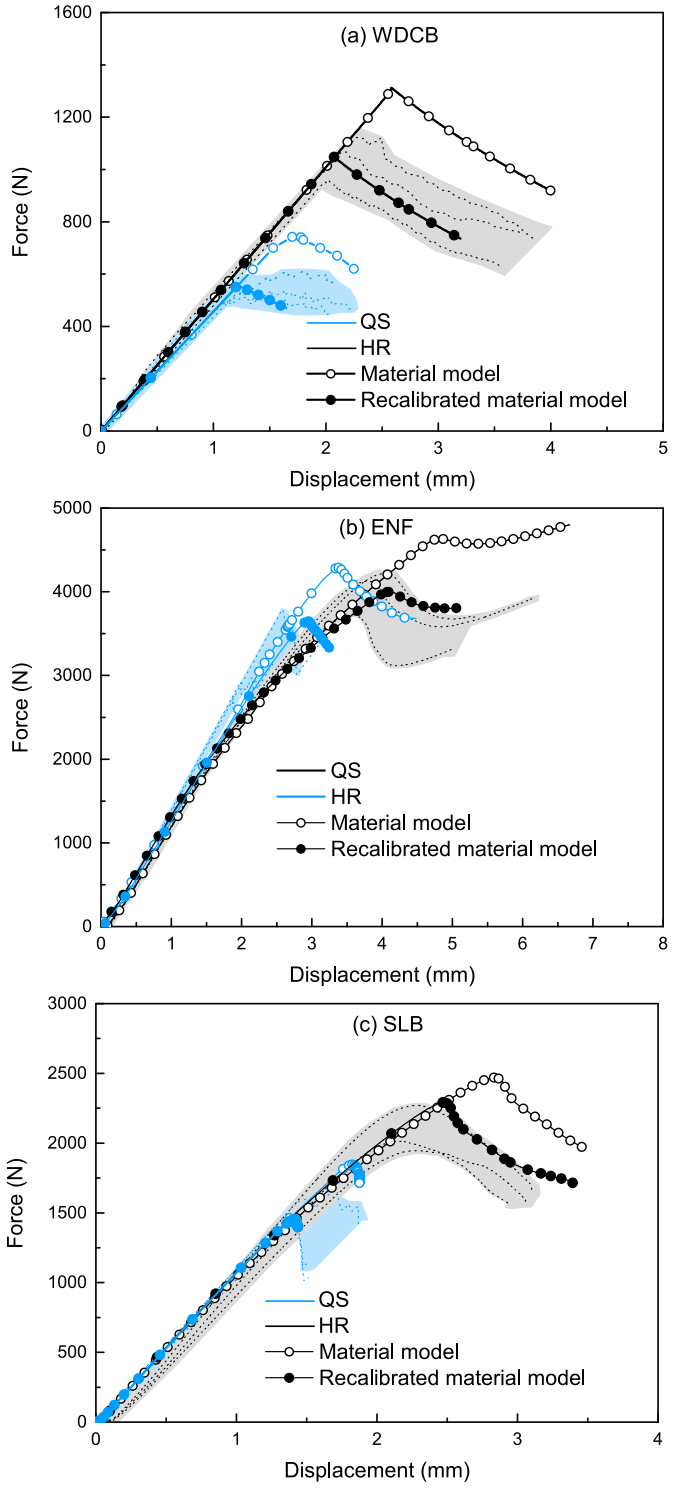

Fig. 20. Representation of the corrected model to predict the experimentally obtained force-displacement curves for a) WDCB, b) ENF and c) SLB specimens.

predominantly cohesive in nature. This gave further validity to the fracture energy results – it is reasonable that these belong to the adhesive interface itself and not the interface between the metal and the adhesive.

5. Numerical modelling of the experiments is used to validate a CZM of the adhesive. This was previously characterised with smaller scale specimens. The simulated results were able to predict the experiments accurately. The combination of small scale experiments and large scale fracture mechanics experiments provide a flexible and powerful framework for the study of adhesives loaded both quasi-statically and dynamically.

Acknowledgements

The authors of this paper are grateful to Jeffrey Fullerton and Stuart Carter, Impact Engineering Laboratory, University of Oxford, for their assistance in the manufacturing of the specimens. The authors acknowledge the funding from Rolls-Royce plc which enabled this investigation.

References

[1] Banea MD, Da Silva LF. Adhesively bonded joints in composite materials: An overview. Proc Inst Mech Eng Part L 2009;223(1):1–18. https://doi.org/10.1243/14644207JMDA219. arXiv:1011.1669v3

[2] Machado JJM, Marques EAS, da Silva LFM. Adhesives and adhesive joints under impact loadings: an overview. J Adhesion 2018;94(6):421–52. https://doi.org/10.1080/00218464.2017.1282349.

[3] Yokoyama T, Shimizu H. Evaluation of impact shear strength of adhesive joints with the split hopkinson bar. JSME Int J 1998;41(4):503–9.

[4] May M, Hesebeck O, Marzi S, Böhme W, Lienhard J, Kilchert S, et al. Rate dependent behavior of crash-optimized adhesives Experimental characterization, model development, and simulation. Eng Fract Mech 2015;133:112–37. https://doi.org/10.1016/j.engfracmech.2014.11.006. http://linkinghub.elsevier.com/retrieve/pii/S0013794414003804

[5] Yokoyama T, Nakai K. Determination of the impact tensile strength of structural adhesive butt joints with a modified split hopkinson pressure bar. Int J Adhesion Adhesiv 2015;56:13–23. https://doi.org/10.1016/j.ijadhadh.2014.07.011.

[6] Yokoyama T. Experimental determination of impact tensile properties of adhesive butt joints with the split Hopkinson bar. J Strain Anal Eng Design 2003;38(3):233–45. https://doi.org/10.1243/030932403765310563. http://journals.pepublishing.com/openurl.asp?genre=article&id=doi:10.1243/030932403765310563

[7] Raykhere SL, Kumar P, Singh R, Parameswaran V. Dynamic shear strength of adhesive joints made of metallic and composite adherents. Mater Design 2010;31(4):2102–9. https://doi.org/10.1016/j.matdes.2009.10.043. http://linkinghub.elsevier.com/retrieve/pii/S0261306909005974

[8] Tsai MY, Morton J. An investigation into the stresses in double-lap adhesive joints with laminated composite adherends. Int J Solid Struct 2010;47(24):3317–25. https://doi.org/10.1016/j.ijsolstr.2010.08.011.

[9] Lißner M, Alabort E, Cui H, Pellegrino A, Petrinic N. On the rate dependent behaviour of epoxy adhesive joints: experimental characterisation and modelling of mode i failure. Compos Struct 2018;189:286–303. https://doi.org/10.1016/j.compstruct.2018.01.019.

[10] Pinto AM, Magalhães AG, Campilho RD, de Moura MF, Baptista AP. Single-lap joints of similar and dissimilar adherends bonded with an acrylic adhesive. J Adhesion 2009;85(6):351–76. https://doi.org/10.1080/00218460902880313.

[11] Sassi S, Tarfaoui M, Yahia HB. Thermomechanical behavior of adhesively bonded joints under out-of-plane dynamic compression loading at high strain rate. J Compos Mater 2018;52(30):4171–84. https://doi.org/10.1177/0021998318777048.

[12] Sassi S, Tarfaoui M, Benyahia H. Experimental study of the out-of-plane dynamic behaviour of adhesively bonded composite joints using split hopkinson pressure bars. J Compos Mater 2018;52(21):2875–85. https://doi.org/10.1177/0021998318758368.

[13] Sassi S, Tarfaoui M, Ben Yahia H. An investigation of in-plane dynamic behavior of adhesively-bonded composite joints under dynamic compression at high strain rate. Compos Struct 2018;191:168–79. https://doi.org/10.1016/j.compstruct.2018.02.057.

[14] Sassi S, Tarfaoui M, Ben Yahia H. In-situ heat dissipation monitoring in adhesively bonded composite joints under dynamic compression loading using SHPB. Compos Part B 2018;154(July):64–76. https://doi.org/10.1016/j.compositesb.2018.07.039.

[15] Lißner M, Alabort E, Cui H, Rito R, Blackman B, Petrinic N. Experimental characterisation and numerical modelling of the influence of bondline thickness, loading rate, and deformation mode on the response of ductile adhesive interfaces. J Mech Phys Solid 2019;130:349–69. https://doi.org/10.1016/j.jmps.2019.06.011.

[16] Blackman BRK, Kinloch AJ, Rodriguez Sanchez FS, Teo WS, Williams JG. The fracture behaviour of structural adhesives under high rates of testing. Eng Fract Mech 2009;76(18):2868–89. https://doi.org/10.1016/j.engfracmech.2009.07.013. http://linkinghub.elsevier.com/retrieve/pii/S0013794409002380

[17] Neumayer J, Kuhn P, Koerber H, Hinterhölzl R. Experimental Determination of the Tensile and Shear Behaviour of Adhesives under Impact Loading. J Adhesion 2015;92(7-9):503–16. https://doi.org/10.1080/00218464.2015.1092387. http://

www.scopus.com/inward/record.url?eid=2-s2.0-84962339117&partnerID=tZOtx3y1
[18] Wiegand J, Hornig A, Gerlach R, Neale C, Petrinic N, Hufenbach W. An experimental method for dynamic delamination analysis of composite materials by impact bending. Mech Adv Mater Struct 2015;22(5):413–21. https://doi.org/10.1080/15376494.2012.736066.
[19] Yasaee M, Mohamed G, Pellegrino A, Petrinic N, Hallett SR. Strain rate dependence of mode II delamination resistance in through thickness reinforced laminated composites. Int J Impact Eng 2017;107(May):1–11. https://doi.org/10.1016/j.ijimpeng.2017.05.003.
[20] Isakov M, May M, Hahn P, Paul H, Nishi M. Fracture toughness measurement without force data application to high rate DCB on CFRP. Compos Part A 2019;119(January):176–87. https://doi.org/10.1016/j.compositesa.2019.01.030.
[21] Ponnusami SA, Pathan MV, Cui H, Erice B, Petrinic N. A wedge-DCB test methodology to characterise high rate mode-I interlaminar fracture properties of fibre composites. EPJ Web Conf 2018;183(January). https://doi.org/10.1051/epjconf/201818302052.
[22] Blackman BRK, Kinloch AJ, Paraschi M, Teo WS. Measuring the mode i adhesive fracture energy, GIC, of structural adhesive joints: the results of an international round-robin. Int J Adhesion Adhesiv 2003;23(4):293–305. https://doi.org/10.1016/S0143-7496(03)00047-2.
[23] Álvarez D, Blackman BRK, Guild FJ, Kinloch AJ. Mode i fracture in adhesively-bonded joints: a mesh-size independent modelling approach using cohesive elements. Eng Fract Mech 2014;115:73–95. https://doi.org/10.1016/j.engfracmech.2013.10.005.
[24] De Moura MF, Dourado N, Morais JJ, Pereira FA. Numerical analysis of the ENF and ELS tests applied to mode II fracture characterization of cortical bone tissue. Fatigue Fract Eng Mater Struct 2011;34(3):149–58. https://doi.org/10.1111/j.1460-2695.2010.01502.x.
[25] Oliveira JM, De Moura MF, Morais JJ. Application of the end loaded split and single-leg bending tests to the mixed-mode fracture characterization of wood. Holzforschung 2009;63(5):597–602. https://doi.org/10.1515/HF.2009.088.
[26] da Silva LFM, Esteves VHC, Chaves FJP. Fracture toughness of a structural adhesive under mixed mode loadings. Materialwissenschaft und Werkstofftechnik 2011;42(5):460–70. https://doi.org/10.1002/mawe.201100808.
[27] Yamagata Y, Lu X, Sekiguchi Y, Sato C. Experimental investigation of mode i fracture energy of adhesively bonded joints under impact loading conditions. Appl Adhesion Sci 2017;5(7):1–10. https://doi.org/10.1186/s40563-017-0087-7.
[28] Dillard DA, Pohlit DJ, Jacob GC, Starbuck JM, Kapania RK. On the use of a driven wedge test to acquire dynamic fracture energies of bonded beam specimens. J Adhesion 2011;87(4):395–423. https://doi.org/10.1080/00218464.2011.562125.
[29] Aurore N, Julien J. Double cantilever beam tests on a viscoelastic adhesive: effects of the loading rate. Procedia Struct Integrit 2016;2:269–76. https://doi.org/10.1016/j.prostr.2016.06.035.
[30] Andersson T, Stigh U. The stress-elongation relation for an adhesive layer loaded in peel using equilibrium of energetic forces. Int J Solid Struct 2004;41(2):413–34. https://doi.org/10.1016/j.ijsolstr.2003.09.039.
[31] Blackman BR, Kinloch AJ, Paraschi M. The determination of the mode II adhesive fracture resistance, GIIC, of structural adhesive joints: an effective crack length approach. Eng Fract Mech 2005;72(6 SPEC. ISS.):877–97. https://doi.org/10.1016/j.engfracmech.2004.08.007.
[32] De Moura MF. Numerical simulation of the ENF test for the mode-II fracture characterization of bonded joints. J Adhesion Sci Technol 2006;20(1):37–52. https://doi.org/10.1163/156856106775212422.
[33] de Moura MF, Silva MA, de Morais AB, Morais JJ. Equivalent crack based mode II fracture characterization of wood. Eng Fract Mech 2006;73(8):978–93. https://doi.org/10.1016/j.engfracmech.2006.01.004.
[34] Alfano M, Link RE, Paulino GH, Pagnotta L, Furgiuele F, Mitchell MR. Analysis of fracture in aluminum joints bonded with a bi-Component epoxy adhesive. J Test Evaluat 2010;39(2):102753. https://doi.org/10.1520/jte102753.
[35] Sarrado C, Turon A, Costa J, Renart J. On the validity of linear elastic fracture mechanics methods to measure the fracture toughness of adhesive joints. Int J Solid Struct 2015;81:110–6. https://doi.org/10.1016/j.ijsolstr.2015.11.016.
[36] Sekiguchi Y, Katano M, Sato C. Experimental study of the mode i adhesive fracture energy in DCB specimens bonded with a polyurethane adhesive. J Adhesion 2017;93(3):235–55. https://doi.org/10.1080/00218464.2015.1070101.
[37] Xavier J, Morais J, Dourado N, De Moura MF. Measurement of mode i and mode II fracture properties of wood-bonded joints. J Adhesion Sci Technol 2012;25(20):2881–95. https://doi.org/10.1163/016942411X576563.
[38] Da Silva LF, De Magalhães FA, Chaves FJ, De Moura MF. Mode II fracture toughness of a brittle and a ductile adhesive as a function of the adhesive thickness. J Adhesion 2010;86(9):889–903. https://doi.org/10.1080/00218464.2010.506155.
[39] de Moura MFSF, Campilho RDSG, Goncalves JPM. Pure mode II fracture characterization of composite bonded joints. Int J Solid Struct 2009;46(6):1589–95. https://doi.org/10.1016/j.ijsolstr.2008.12.001.
[40] Ducept F, Davies P, Gamby D. Mixed mode failure criteria for a glass/epoxy composite and an adhesively bonded composite/composite joint. Int J Adhesion Adhesiv 2000;20(3):233–44. https://doi.org/10.1016/S0143-7496(99)00048-2.
[41] Fernlund G, Spelt JK. Mixed-mode fracture characterization of adhesive joints. Compos Sci Technol 1994;50(4):441–9. https://doi.org/10.1016/0266-3538(94)90052-3.
[42] Gledhill RA, Kinloch AJ, Yamini S, Young RJ. Relationship between mechanical properties of and crack progogation in epoxy resin adhesives. Polymer 1978;19(5):574–82. https://doi.org/10.1016/0032-3861(78)90285-9.
[43] Kinloch AJ, Shaw SJ. The fracture resistance of a toughened epoxy adhesive. J Adhesion 1981;12(1):59–77. https://doi.org/10.1080/00218468108071189.
[44] Kanninen MF, Popelar CH. Advanced Fracture Mechanics. New York: Oxford Science Publication; 1985.
[45] Ding W. Delamination Analysis of Composite Laminates. University of Toronto; 1999.
[46] Wang Y, Williams JG. Corrections for mode II fracture toughness specimens of composites materials. Compos Sci Technol 1992;43(3):251–6. https://doi.org/10.1016/0266-3538(92)90096-L.
[47] Budzik MK, Jumel J, Ben Salem N, Shanahan ME. Instrumented end notched flexure - Crack propagation and process zone monitoring part II: data reduction and experimental. Int J Solid Struct 2013;50(2):310–9. https://doi.org/10.1016/j.ijsolstr.2012.08.030.
[48] Ben Salem N, Jumel J, Budzik MK, Shanahan ME, Lavelle F. Analytical and experimental investigations of crack propagation in adhesively bonded joints with the mixed mode bending (MMB) test part i: macroscopic analysis & digital image correlation measurements. Theor Appl Fract Mech 2014;74(1):209–21. https://doi.org/10.1016/j.tafmec.2014.05.006.
[49] Cui H. Delamination and Debonding Failure of Laminated Composite T-joints. TU Delft; 2014.
[50] Marzi S, Biel A, Stigh U. On experimental methods to investigate the effect of layer thickness on the fracture behavior of adhesively bonded joints. Int J Adhesion Adhesiv 2011;31(8):840–50. https://doi.org/10.1016/j.ijadhadh.2011.08.004.
[51] Alvarez Feito D. Fracture Mechanics of Carbon Fibre Reinforced Plastics to Ti-alloy Adhesive Joints. Imperial College London; 2012.
[52] Delvare F, Hanus JL, Bailly P. A non-equilibrium approach to processing hopkinson bar bending test data: application to quasi-brittle materials. Int J Impact Eng 2010;37(12):1170–9. https://doi.org/10.1016/j.ijimpeng.2010.07.001.